ACS Catalysis

pubs.acs.org/acscatalysis
Research Article

Dynamic Surface Restructuring and Carbonate-Mediated Pathways in Perovskite-Catalyzed CO Oxidation Revealed by Operando Spectroscopy

Nicolas Cosanne,[‡] Daniel Cruz,[‡] Pierfrancesco Ticali, Hamidreza Hajiyani, Shilong Chen,[†] Patrick Zeller, Thomas Götsch, Alexander Klyushin, Axel Knop-Gericke, Martin Muhler, Beatriz Roldan Cuenya, Robert Schlögl, Malte Behrens, and Sharif Najafishirtari*

Cite This: ACS Catal. 2026, 16, 12062−12079
Read Online

ACCESS | Metrics & More | Article Recommendations | Supporting Information

ABSTRACT: The perovskite-based catalysts $LaFeO_3$ (LFO) and $LaFe_{0.75}Co_{0.25}O_3$ (LFCO) were examined to elucidate the reaction mechanism and disentangle the complex surface phenomena occurring during the seemingly simple CO oxidation reaction. Precise kinetic measurements and operando spectroscopy were employed to explain the interplay between the formation of surface intermediates and the transformations of the surface sites, leading to the occurrence of a frustrated-phase transition at the surface that can potentially define the catalyst activity under different reaction conditions. Our work specifically highlights the effect of partial cobalt substitution into the perovskite's structure on improving the activity of the reference LFO. Modulation-excitation spectroscopy coupled with phase-sensitive detection (MES-PSD) and near-ambient pressure X-ray photoelectron spectroscopy (NAP-XPS) were employed at different temperatures to elucidate the multifaceted role of cobalt in promoting the carbonate-mediated pathway for CO oxidation. For LFO, kinetic and theoretical analyses confirm a pure Mars–van Krevelen (MvK) mechanism mediated by bidentate carbonates, yielding low activity but high stability. In contrast, LFCO exhibits higher activity despite slight deactivation through a dual MvK/Langmuir–Hinshelwood (LH) pathway. Monodentate carbonates act as low-temperature and unstable intermediates, with LFCO accelerating carbonate-to-CO_2 conversion via enhanced surface oxygen mobility. The temperature also dictates mechanistic shifts: LH dominates below 170 °C, while MvK prevails above this threshold. Additionally, operando NAP-XPS reveals that this transition coincides with cobalt reduction, iron oxidation, and a possible frustrated-phase transition that activates carbonate intermediates. In our catalytic systems, cobalt serves as the primary active site, while lanthanum stabilizes the perovskite structure and surface carbonates, and iron maintains charge balance. The interplay between the sites is essential to achieve a higher conversion. These findings demonstrate how composition and temperature govern dynamic surface restructuring and reaction pathways in perovskite catalysts.

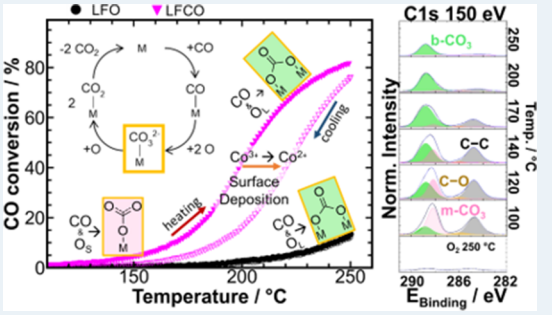

KEYWORDS: *CO oxidation, perovskite catalysts, operando spectroscopy, reaction mechanism, frustrated-phase transition, DRIFTS, MES, NAP-XPS*

1. INTRODUCTION

CO oxidation is a simple and extensively studied probe reaction over various metal catalysts, such as gold,[1,2] silver,[3] platinum,[4] or even bimetallic phases, such as cobalt–palladium.[5] Due to the rising cost of noble and rare-earth metals, transition metal oxides, such as CuO,[6] $LaFeO_3$,[7] Co_3O_4,[8] and other spinel catalysts,[9] have also been recently studied. CO oxidation to CO_2 is considered a straightforward reaction (eq 1), in which no other gas-phase by-products are formed. On metal catalysts, usually, a Langmuir–Hinshelwood mechanism is reported for this reaction, which requires adsorbed CO and adsorbed atomic oxygen to be in proximity to each other on the surface.[10]

$$2\,CO + O_2 \rightleftharpoons 2\,CO_2 \quad (1)$$

Received: February 19, 2026
Revised: May 22, 2026
Accepted: May 26, 2026
Published: June 15, 2026

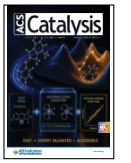

https://doi.org/10.1021/acscatal.6c01338
ACS Catal. 2026, 16, 12062−12079

On the other hand, a Mars–van Krevelen mechanism can be observed for reducible oxide catalysts, as described by Liu et al. for Co-doped CeO_2.[11] Here, two pathways are possible: either a direct pathway (pathway A) or an indirect one (pathway B), as schematically displayed in Scheme 1. In pathway A, oxygen vacancies are formed due to the reaction of adsorbed CO and lattice oxygen, $O_{(l)}$, to adsorbed CO_2. This is also in good accordance with reported CO oxidation mechanisms over $SrCoO_3$,[12] $SrFeO_3$,[13] and Fe_3O_4.[14]

The other reported possibility is a reaction pathway involving carbonates[11] as reaction intermediates, which are often overlooked. Carbonates can react with another CO molecule on the surface, forming two CO_2 molecules. The CO_2 molecules desorb, leaving two oxygen vacancies, which can be filled by dissociative adsorption of O_2. Similarly, active carbonate species have also been reported on Cu_xO/CeO_2,[15] Ag-Pt nanoparticles,[16] and in multiple instances on Pt/Al_2O_3.[17−19] Here, the carbonates are reported to decompose to CO_2, leaving surface oxygen behind. Because carbonates are also formed as byproducts from CO_2 on the surface in pathway A,[10] thereby poisoning active sites, the presence of carbonates alone is not an indication of a carbonate-facilitated pathway, making the distinction difficult. An example of this can be seen in one of our previous studies, where the high intensity of the carbonate species makes it hard to follow the kinetics of the reaction.[7] Similarly, the carbonates were also reported on Rh(111) single crystals after deactivation and poisoning the surface, especially when hydroxyl groups were present on the surface.[20]

Indeed, characterizing the reaction intermediates, even for a so-called "simple" reaction such as CO oxidation, is an important part of understanding catalytic mechanisms to optimize catalysts and fine-tune them for a specific reaction. It is generally difficult to isolate and detect intermediates for further analysis, considering their typical very reactive and unstable nature. While techniques exist to probe adsorbed species on the catalyst surface during a reaction, such as diffuse reflectance infrared Fourier transform spectroscopy (DRIFTS),[21,22] Raman spectroscopy, or X-ray photoelectron spectroscopy (XPS), it is challenging to differentiate between active and non-active adsorbates (spectators) since both are present on the surface. Spectators, in contrast to the reactive intermediates, do not play a role in the formation of the desired reaction products. Due to their accumulation on the surface, they can block access to the active sites, thereby deactivating the catalyst by reducing the number of available active sites. A powerful tool to differentiate between active and spectator species is modulation excitation spectroscopy (MES) coupled with DRIFTS using phase-sensitive detection (PSD). This technique enables the elimination of spectators from the spectra and, therefore, allows the study of only reactive components.[23] Furthermore, information derived from MES experiments contains kinetic information, which can be used to elaborate on the reaction mechanism and the role of different surface species.[23] Operando DRIFTS could additionally be coupled with isotope experiments, such as steady-state isotopic transient kinetic analysis (SSITIKA),[24] to generate additional kinetic information of the active intermediates and the product distribution.[25,26]

In this work, we applied MES-PSD coupled with DRIFTS to examine two oxide samples, representing active and inactive catalysts. Additionally, operando near-ambient pressure X-ray photoelectron spectroscopy (NAP-XPS) was used to elucidate the role of reactive carbonates in the more active catalyst. We

Scheme 1. Schematic Representation of Two Possible Mechanisms of CO Oxidation on a Catalyst Surface[a]

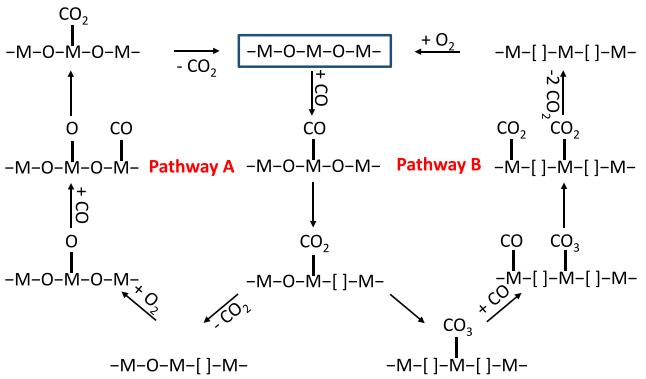

[a]Pathway A represents a direct conversion of CO and O_2 to CO_2, while pathway B shows a mechanism where carbonates are formed as intermediates. Mechanisms are inspired by Liu et al.,[11] with permission from the Royal Society of Chemistry, Copyright, 2018.

focused on the lanthanum–iron–cobalt perovskite $LaFe_{1-x}Co_xO_3$ samples previously applied by our group in the CO oxidation.[7] Perovskites (ABO_3) are a well-suited material for spectroscopic analysis due to their well-defined structure. The defined orthorhombic structure of $LaFeO_3$ contains a dodecahedrally coordinated A-site cation, lanthanum in this case, and an octahedrally coordinated B-site cation, iron. While completely substituting iron with cobalt would lead to a rhombohedral structure, with our synthesis method, up to 25% of cobalt can be substituted into the structure while maintaining phase-pure.[27,28] Therefore, iron and cobalt are present in the same coordination and oxidation states in the material, allowing for a comparison of both cations without any other changes to the material. The aforementioned structural comparison is, however, only valid for the as-prepared catalyst. It is well known that most catalysts experience changes during their time on stream and deactivate.[29−31] If such a change includes the change of the surface phase, it is, however, possible that the catalyst is activated during this process. Due to this new phase being energetically unstable, it was described as frustrated by Schögl.[28,32] Lunkenbein and co-workers even described it as a frustrated-phase transition.[33] In this case, the surface sites and structure change to a more active state under reaction conditions due to the formation of oxygen vacancies, resulting in the catalyst trying to re-establish its more stable form. As long as the catalyst returns to its initial state and is not completely decomposed into La_2O_3 and FeO/CoO during this mechanism, it is thereby stuck in a loop of this frustrated-phase transition. Determining if this transition is due to the formation of oxygen vacancies and/or redox changes and the interaction of the reaction intermediates with the surface structure, is a key point in catalysis research.[32] Two $LaFe_{1-x}Co_xO_3$ samples were studied, labeled LFO, *i.e.*, $x = 0\%$ (0% cobalt) as a reference of low activity, and LFCO, *i.e.*, $x = 25\%$ (25% cobalt) as the more active sample. The reproduced catalysts were characterized via powder X-ray diffraction (PXRD), ion-coupled plasma optical emission spectroscopy (ICP-OES), N_2-physisorption after Brunauer, Emmett, and Teller (BET), Raman spectroscopy, NH_3 temperature-programmed desorption (NH_3-TPD), and scanning electron microscopy (SEM). We focused our attention on steady-state

https://doi.org/10.1021/acscatal.6c01338
ACS Catal. 2026, 16, 12062−12079

gas-phase experiments to calculate apparent activation energies and reaction orders using a power rate law equation. These results were complemented by density functional theory (DFT + U) calculations of the reaction pathway of CO to CO_2 over both LFO and LFCO. Both mechanisms were also calculated with and without surface O_2. We employed operando DRIFTS in combination with modulation excitation and phase-sensitive detection (DRIFT-MES-PSD) coupled with a mass spectrometer (MS) to analyze the intermediates and kinetics of the reaction over the catalysts. Operando near-ambient pressure X-ray photoelectron spectroscopy (NAP-XPS) and X-ray absorption near-edge spectroscopy (XANES) results were additionally used to monitor changes in the LFCO catalyst's surface and the oxidation states of the different cations to find the active sites, as well as the distribution of different carbonates and oxygen-containing intermediates on the surface.

2. EXPERIMENTAL METHODS

2.1. Synthesis

The catalysts were prepared according to a method reported by Dreyeret al.[7,27] using an automated lab reactor OptiMax 1001 (Mettler Toledo) and washed by centrifugation with distilled water until the conductivity was below 100 μS. Iron(III) nitrate nonahydrate (Sigma-Aldrich, >98% purity), lanthanum(III) nitrate hexahydrate (abcr, 99.9% purity), cobalt(II) nitrate hexa-hydrate (Gruening, 99% purity), sodium hydroxide (Gruening, 99% purity), and sodium carbonate (Gruening, 99.5% purity) were used to precipitate the precursor.

The precipitates were then dried in air at 80 °C overnight and subsequently calcined at 800 °C for 3 h at a heating rate of 2 K min^{-1} in a Nabertherm B150 muffle furnace in static air.

2.1.1. X-Ray Diffraction. The crystal structure and phase purity were determined by PXRD within the 2θ angle range of 2 ° to 40 ° on molybdenum Kα radiation. The samples were placed between Scotch tape and measured in transmission mode on a *STADI-P* by *Stoe* with a *MYTHEN 1 K* detector and a germanium (111) monochromator.

2.1.2. Inductively Coupled Plasma-Optical Emission Spectroscopy (ICP-OES). The La, Co, and Fe contents were determined by ICP-OES. Samples were measured on an *Avio 200 ICP Optical Emission Spectrometer* with a *PerkinElmer S23* autosampler. The samples were dissolved by heating 5 mL of 68% concentrated HNO_3 and subsequently filled up to 50 mL with distilled water. Prior to the ICP-OES measurement, the sample was further diluted with distilled water using a ratio of 1:10. The samples were automatically measured three times to determine error values.

2.1.3. N_2–Physisorption. To determine the surface area, N_2–physisorption according to the BET method was employed. 100 mg of catalyst was loaded into a quartz tube and pretreated under vacuum at 80 °C for 2 h to degas and completely dry the surface. After degassing, the catalysts were weighed again and then loaded into a *NOVA 300* (*Quantachrome GMbH*) for measurement. Surface areas and pore size distributions were calculated by the software *NovaWin* of the device according to the BET and BJH methods, respectively.

2.1.4. Electron Microscopy. Scanning electron microscopy (SEM) was used to determine particle morphology and size employing an SEM *Ultra 55 Plus* with the *SmartSEM 5.04* software by *ZEISS*.

2.1.5. NH_3-TPD. NH_3 temperature-programmed desorption (NH_3-TPD) experiments for obtaining information on catalyst acidity were performed in a *BELCAT-II* (*BEL Japan, Inc.*) at a linear heating rate of 6 °C min^{-1} between 40 and 600 °C, followed by an isothermal dwell of 30 min. The samples (around 60 mg for each sample) were isothermally heated at 120 °C for 1 h in Ar (80 Ncc min^{-1}, Ar ≥ 99.999%, *Air Liquide*) before the experiments and purged with argon during cooling to 40 °C. The atmosphere was switched from Ar to 3% NH_3/Ar (80 Ncc min^{-1}, NH_3 ≥ 99.999%, Ar ≥ 99.999%, *Air Liquide*) at 40 °C and kept in the ammonia gas mixture for adsorption for 1 h. Afterward, the sample was purged by Ar at 40 °C for 90 min to remove gas-phase NH_3 and physisorbed NH_3. Then, the samples were heated in Ar (60 Ncc min^{-1}) to 600 °C and the NH_3 content (mass = 17) in the exhaust was monitored by a mass spectrometer (*QMG 220, Pfeiffer Vacuum GmbH*).

2.1.6. RAMAN Spectroscopy. RAMAN spectra were recorded with a *LabRAM HR Evolution* by *Horiba Scientific*. Spectra were recorded with a green laser (λ=532 nm) with 1% laser intensity (max. 100 mW). Each sample was put on a slide, and the laser was focused with a 100× lens. The spectra were recorded for 10 min with two accumulations to filter out potential radiation spikes.

2.2. Catalytic Testing

CO oxidation was carried out in a home-built setup described elsewhere[27] and in the SI.

The catalysts were first heated from 50 to 250 °C in 25 Scc min^{-1} pure O_2 (*Westfalen*, 99.999%) at a heating ramp of 5 K min^{-1}. After a holding time of 120 min, the catalyst was cooled to 50 °C and purged for 15 min with 100 Scc min^{-1} N_2 (evaporated from liquid N_2 and filtered by an SGT triple filter removing moisture, hydrocarbons, and CO_2). This process is referred to as TPO, *i.e.*, temperature-programmed oxidation. Next, the lines were purged with the reactive mixture of 2% CO (*Air Liquid*, 19.91 Vol% ± 0.40 Vol% in N_2) and 1% O_2 in N_2 (100 Scc min^{-1}) for 15 min. The catalyst was then heated to 100, 120, 140, 170, 200, and 250 °C consecutively with a heating rate of 2 K min^{-1} and a dwell time of 120 min. After cooling to 50 °C and flushing for 15 min with first N_2 and then pure O_2, another TPO was performed to regenerate the catalyst. Thereafter, the transient measurements were performed by switching the feed to the reaction mixture, dwelling for 15 min, and heating to 250 °C with a rate of 1 K min^{-1} and dwelling at this temperature for 60 min before cooling to 50 °C again. The TPO and transient measurements were repeated twice more with the same steps as described above. As a last step, the catalysts were heated to 200 °C at a heating rate of 5 K min^{-1} under reactive conditions. This temperature was held for 10 h to fully equilibrate the catalyst and ensure steady-state conditions before cooling to 50 °C again and purging with N_2.

The transient measurements were performed before conducting the steady-state measurements. To ensure kinetically controlled measurements and comparing the catalysts at similar conversions, the temperatures were chosen from the cooling path to ensure a conversion between 2 and 15%. The steady-state experiments were then performed under reaction conditions with six temperature steps per catalyst, each held for 5 h and heating rates of 2 K min^{-1}. For LFO, the temperatures were set to 200, 210, 220, 230, 240, and 250 °C, while LFCO was measured at 160, 165, 170, 175, 180, and 185 °C. These steady-state results were used to calculate apparent activation energies. Afterward, the catalysts were also tested in a range of reactant mixtures by varying the oxygen content first from 0.8 to 1.2% in 0.1% steps while keeping the CO content at 2%. The CO content was varied from 1.8 to 2.2% in 0.1% steps while O_2 was kept stable at 1%. This test was conducted at ∼10% conversion for both catalysts (at 180 °C for LFO and 220 °C for LFCO) and used to apply the power rate law equation to calculate reaction orders of CO and O_2.

For further stability measurements, transient measurements of LFO were conducted, each after a TPO, as described above, but up to temperatures of 250, 300, 350, and 400 °C, respectively. Furthermore, after another TPO, LFO was heated to 350 °C for 10 h (5 K min^{-1}) under reactive conditions. The same 10 h experiment was performed for LFCO but at 250 °C.

2.3. DRIFTS-MES

DRIFTS was performed using a *ThermoFisher Nicolet iS20* FTIR spectrometer equipped with a liquid nitrogen-cooled mercury cadmium

https://doi.org/10.1021/acscatal.6c01338
ACS Catal. 2026, 16, 12062−12079

telluride detector (MCT) and a *Praying Mantis* high-temperature reaction chamber unit (from *Harrick Scientific Products Inc.*). A *Ministat 125* by *HUBER* was used to provide circulating cooling water (8 °C) to protect the external part of the reaction chamber. All time-series data were recorded using the Gram-Schmidt method, and the *OMNIC* measurement program automatically recorded the basis vectors. The time-resolved spectra were baseline-corrected and converted to Kubelka–Munk units. No atmospheric compensation was considered for the data processing to avoid introducing signal artifacts as the device was also continuously purged by a H_2O- and CO_2-free N_2 stream.

To feed the gas into the DRIFTS cell, a home-built dosing unit was used. The setup provides two different streams, which can be controlled individually at the same time (stream A and stream B). A maximum gas flow of 80 Scc min^{-1} per stream was applied. The DRIFTS cell was loaded with 40 mg of catalyst (<250 μm) on top of quartz wool. During the preparation, the catalyst surface is made as flat as possible. After the reaction, the gas flow was sent to an *OMNISTAR GSD 320* mass spectrometer by *Pfeifer Vacuum* with the "flow through" mode so that the gas was collected after passing through the catalyst bed.

During the measurements, the samples were first pretreated with a TPO at 350 °C with 20% O_2 (*Westfalen*, 99.999%) in He (*Westfalen*, 99.999%) for 60 min at a heating rate of 10 K min^{-1}. They were then cooled to 200 °C and purged in He for 10 min. After collecting the background, the first MES measurement was started. Stream A was set to reaction conditions of 0.5% CO (*Air Liquid*, 19.91 Vol% ± 0.40 Vol% in N_2) and 0.25% O_2, and stream B was pure He. The spectra were collected during 20 cycles, exposing the catalyst alternately to streams A or B, representing the two half-periods of stimulation and relaxation. In each half-period, 30 spectra were collected with a 5 s step size per spectrum and 5 scans per spectrum. A TPO was then performed to regenerate the catalyst. MES measurements were additionally conducted at 100, 120, and 150 °C for both catalysts using the same protocol.

After reaching the quasi-steady state at the 10th cycle, the corresponding spectra of the last 10 cycles were averaged to increase the signal-to-noise ratio and the resulting 60 time-resolved spectra were transformed into the phase domain according to the following equation (eq 2):[23,34]

$$A_k\left(\varphi_k^{PSD}\right) = \frac{2}{\tau}\int_0^{\tau} A(t)\sin\left(k\omega t + \varphi_k^{PSD}\right)dt \quad (2)$$

where k is the demodulation index, φ_k^{PSD} is the demodulation phase angle for $k\omega$ demodulation, and τ is the time length of a period, while $A(t)$ and $A_k(\varphi_k^{PSD})$ are the responses of the active species in the time and phase domains, respectively.[23]

Phase-sensitive detection (PSD) was performed by finding the in-phase angles, *i.e.*, those φ^{PSD} maximizing the right side of eq 3.[35]

$$A\left(\varphi_k^{PSD}\right) = A\cos\left(\phi - \varphi^{PSD}\right) \quad (3)$$

To investigate the kinetics and the mechanism behind the process, the PSD analysis was performed at different $k\omega$ demodulation indices, *i.e.*, k = 1, 3, 5, 7, and 9.[23,35−38]

2.4. NAP-XPS/XANES Experiments

NAP-XPS/XANES measurements were conducted at the *Berlin Joint Lab for Electrochemical Interfaces* (*BEIChem*) with an elliptical undulator *UE56/2-PGM1* of the *BESSY II* electron storage ring operated by the Helmholtz-Zentrum Berlin für Materialien und Energie. The experiments utilized a specialized *SPECS GmbH Phoibos 150* electron analyzer, specifically designed to operate under near-ambient pressure conditions. To separate the UHV system of the beamline and the reaction atmosphere in the reaction cell, a thin silicon nitride (SiNx, 50 nm thick) membrane was installed close to the sample, and electron collection was facilitated by a differentially pumped analyzer equipped with electrostatic focusing lenses.

Samples of perovskite LFCO prepared as powder pellets with 60 mg were positioned on a sapphire holder alongside a K-type thermocouple for accurate temperature monitoring. The holder assembly was installed inside the NAP-XPS/XANES chamber near the differential pumping aperture. Sample heating was performed from the backside using an infrared laser, and the gas-phase composition during catalytic conversion was continuously monitored using a quadrupole mass spectrometer. A complete description of this instrumentation and setup can be found elsewhere.[39,40]

Prior to the measurements, all samples were thermally pretreated under an O_2 atmosphere (0.5 mbar O_2) at 250 °C (heating rate 5 K min^{-1}) to remove adsorbed carbonaceous impurities. Following the pretreatment, the samples were exposed to a reaction gas mixture consisting of CO, O_2, and Ar (total pressure: 0.25 mbar), with a 1:1 CO:O_2 ratio (flow rates: 1 Ncc min^{-1} CO, 1 Ncc min^{-1} O_2, and 0.15 Ncc min^{-1} Ar). CO oxidation was studied by progressively increasing the sample temperature from 100 °C to 250 °C. At each temperature step, the system was allowed to stabilize for 20 min to ensure steady-state conditions before initiating spectroscopic measurements.

Core-level X-ray photoelectron spectroscopy (XPS) spectra were acquired at kinetic energies of 150 eV and 450 eV. Operando soft-X-ray L-edge XANES spectra were collected at near-ambient pressure (0.25 mbar CO:O_2 = 1:1) in the same SPECS Phoibos 150 reaction cell used for NAP-XPS, with simultaneous mass-spectrometric monitoring of catalytic conversion. These measurements were conducted using both Auger electron yield (AEY) for surface-sensitive measurements and total electron yield (TEY) for subsurface-sensitive measurements. Normalization of the XANES spectra for Co and Fe L-edges was carried out using the *Athena* software package.[41]

XPS data analysis was performed using *CasaXPS*. Binding energies were calibrated against the Fermi edge of a Pd reference. The Fe 2p, Co 2p, O 1s, and C 1s regions were fitted using mixed Gaussian−Lorentzian line shapes, following Shirley plus linear background subtraction. Details of the peak-fitting parameters and constraints are provided in Tables S1–S6.

Spectral intensities were normalized based on elemental photoionization cross sections, the photon flux at each excitation energy, and the corresponding asymmetry factors. For the quantification of surface species, normalized areas were calculated by dividing the integrated area of each species by the total summed intensity of the relevant core levels. Error bars were included by the uncertainties in the fitted parameters, which were estimated via Monte Carlo simulations implemented in *CasaXPS*.

2.5. DFT Calculations

For simulating the CO oxidation process, we adopted the density functional theory calculations with the Hubbard U term, implemented in CASTEP, the Cambridge Sequential Total Energy Package of Material Studio.[42,43] The bulk properties of $LaFe_{1-x}Co_xO_3$, such as cation ordering, oxidation states, and magnetic configurations, were adopted from the work of Füngerlings et al.[44] An S plane wave cutoff of 530 eV and the effective Hubbard parameters of 4 eV Fe and 3.3 eV for Co were used. A 4 × 4 × 4 Monkhorst-Pack k-point was employed for bulk calculations, while a 2 × 2 × 2 pseudocubic unit cell mesh was used for surface calculations. To avoid interaction between periodic images, a vacuum layer of around 15 Å was inserted between slabs along the z-direction. All systems were relaxed for the residual forces lower than 0.01 eV/Å.

3. RESULTS AND DISCUSSION

3.1. Catalyst Characterization

The catalysts used in this study were prepared using a precipitation route reported elsewhere.[7] Briefly, the precursors were

https://doi.org/10.1021/acscatal.6c01338
ACS Catal. 2026, 16, 12062−12079

synthesized via co-precipitation of the lanthanum, iron, and cobalt nitrates with a mixture of sodium hydroxide and carbonate as the base. Following precipitation, the precursors were calcined at 800 °C to form the desired perovskites. The collected XRD patterns of the synthesized perovskites show no additional reflections and are in good agreement with the $LaFeO_3$ reference, as can be seen in Figure S1a. The expected shift to lower reflection angles due to the substitution of iron with cobalt is also observed for the 25% cobalt sample. The ICP-OES, surface area, and particle size results are summarized in Table 1.

ICP-OES reveals a slightly lower cobalt content for the LFCO sample, with the (Co + Fe)/La ratio higher than one, indicating a less stoichiometric La content compared with that of the theoretical formula. This could be due to the tendency of perovskite materials to form oxygen and cationic vacancies on the A-site.[45,46] The particles resembled sintered and slightly deformed spheres. Cobalt incorporation led to slightly larger particles (Figure S1b) and a lower BET surface area (see Figure S2a–c for details). The surface acidity was analyzed using the NH_3-TPD experiment, which revealed that cobalt incorporation expectedly resulted in a more basic surface (Figure S2d). The measured acidity concerns both Brønsted and Lewis sites since NH_3 cannot differentiate them and binds to both. Raman spectra (Figure S3) revealed a literature-known pattern for LFO,[47−49] with visible modes for the A-site cations and oxygen tilt, bend, and stretch vibrations. Second-order oxygen vibrations were also observed. Upon cobalt substitution, the bands associated with the A-site, oxygen stretch, and 2nd order oxygen vibrations are shifted to lower Raman shifts, while those for the oxygen tilt are shifted to higher Raman shifts, as reported in the literature.[49] Furthermore, the oxygen stretch and bending modes showed an increased intensity, possibly highlighting a higher oxygen vacancy concentration in LFCO.[49]

3.2. Catalytic Testing

Three transient runs were initially performed with one batch of each catalyst (Figure S4). The LFO sample was less active and reached 17% conversion at 250 °C, while the LFCO sample showed 85% conversion. LFCO starts converting CO at 150 °C, and LFO's light-off curve starts at 200 °C. A hysteresis was observed between the heating and cooling segments of the experiment for LFCO after holding the temperature at 250 °C for 1 h. During this holding time, CO conversion and CO_2 yield decrease almost linearly by ∼5%. (Figure S5). This behavior can be attributed to deactivation, which is most likely due to a combination of cobalt reduction and the accumulation of carbonates on the surface.[7,27,32] Since the C-balance is stable at 98% while the catalytic activity decreases, the activity drop is not due to an increase in carbonate formation, but rather in part to the formation of carbonates blocking the active sites. The most active state during the heating segment can be restored via temperature-programmed oxidation (TPO), which removes surface species and reoxidizes the surface, restoring the initial state of the calcined catalysts (Figure S4).

As the deactivation of LFO was not observed at low conversions, additional transient experiments were performed at temperatures up to 300, 350, and 400 °C (Figure S6a). These experiments revealed that even at 90% conversion (400 °C), the LFO catalyst does not show a hysteresis between heating and cooling and, therefore, is not deactivated. This was further confirmed by two stability tests performed on both catalysts at a conversion of 80% after TPO (Figure S6b). While the LFCO catalyst loses around 20% conversion in the first 2 h on stream at 250 °C, the LFO catalyst is much less deactivated in the recorded 10 h time period at 350 °C. While LFCO is still more active at all temperatures above 150 °C than LFO even after deactivation, these experiments show that the iron sites are more resistant to deactivation than the cobalt sites, possibly due to being less prone to reduction.

To further investigate the impact of cobalt substitution and to study the working catalyst at a steady state, the catalysts were preconditioned in the reactive gas feed for 10 h at 200 °C after a transient run, where they had already experienced the reaction temperatures of 250 °C for 1 h. Therefore, the loss of activity during 10 h was small, and it could be concluded that a steady state was reached (Figure S7). Two kinds of steady-state measurements were conducted: (1) a temperature variation test to calculate activation energies and (2) a concentration variation test to calculate the reaction orders based on the power rate law[50] formulation (Figure S8). The corresponding Arrhenius fits are reported in Figure 1a, together with the calculated activation energies. When comparing the two catalysts, the activation energy of LFCO is slightly higher than that of LFO. This could possibly be due to the promotion of the thermal decomposition of the carbonates in the high temperature range used in the case of LFO. Still, considering the calculated error, the activation energies are relatively similar, suggesting the same rate-determining step for both catalysts.

The reaction orders for CO and O_2 were also calculated by the power rate law (see Figure 1b). For the reaction order of CO, the LFO catalyst shows twice as high a value as LFCO, suggesting that the reaction is more affected by the CO concentration. The oxygen reaction order shows a more interesting trend. While the LFCO catalyst has the same reaction order for oxygen as it does for CO, amounting to 0.3, LFO shows a reaction order equal to zero. This suggests that in the absence of cobalt, the reaction follows the Mars–van Krevelen (MvK) type mechanism, while the adsorbed oxygen species on LFCO also play a role in a possible additional contribution from a Langmuir–Hinshelwood (LH) type reaction. However, the contributions of the MvK-type mechanism cannot be excluded by our results for LFCO, similar to a literature report on $SrCoO_3$.[12]

These results still cannot confirm whether pathway A or pathway B (Scheme 1) type mechanism occurs on the catalysts. However, they reveal that on LFO, we have the MvK-type mechanism solely, while the introduction of cobalt allows for the participation of oxygen adsorption in the rate-determining step and a mixed mechanism of MvK and LH. The previously observed lower deactivation of LFO could also be explained by the regeneration of LFO with oxygen, while on LFCO, the stoichiometric amount of oxygen in the feed reacts with CO on the surface. Furthermore, oxygen vacancies can be seen to favor carbonate formation according to pathway B of the MvK type mechanism, while on pathway A, adsorbed oxygen is also directly reacting with CO on the surface. The catalytic results, therefore, suggest a mixed MvK-and LH- type mechanisms corresponding to pathways A and B on LFCO, while on LFO, a pure MvK type mechanism according to pathway B is postulated.

3.3. DRIFTS-MES

3.3.1. Time-Resolved Operando DRIFTS Spectra. To analyze the species formed upon exposing the catalyst to the reaction mixture and during the reaction, both LFO and

https://doi.org/10.1021/acscatal.6c01338
ACS Catal. 2026, 16, 12062−12079

Table 1. Catalyst Characterization via BET, SEM, and ICP-OES[a]

catalysts	a_{BET} / m^2/g	d_{SEM} / nm	n[(Co+Fe)/La] / %	n(Co/Co+Fe) / %
LFO	16	56±14	102±2.6	0
LFCO	9	81 ± 18	109 ± 1.3	23±0.3

[a]d_{SEM} error based on particle size distribution (see Figures S1b and S2a–c for more details).

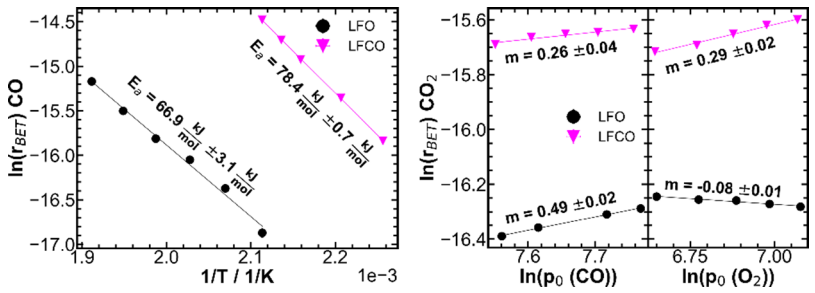

Figure 1. Activation energies (E_a) for CO calculated via Arrhenius (R^2 = 0.991 LFO and 1 LFCO) from steady-state experiments after an additional pretreatment of the catalysts (left) and reaction orders (m) of CO (R^2 = 0.997 LFO and 0.935 LFCO) and O_2 (R^2 = 0.965 LFO and 0.987 LFCO) based on the CO_2 rate (right).

LFCO catalysts were studied using DRIFTS-MES. The first set of measurements was carried out in the reaction mixture (CO + O_2) to study the formation of surface species (*e.g.*, carbonates) by collecting the spectra over time under modulation conditions, *i.e.*, switching between the reaction mixture and inert streams at 100, 120, 150, and 200 °C. During all experiments, the outlet stream of the DRIFTS cell was monitored by a mass spectrometer, proving the approach to quasi-steady-state conditions (as shown exemplarily for the lowest and highest temperatures in Figure S9). The comparison aimed at distinguishing the influence of cobalt inclusion in the system at different temperatures and thus activity levels. The time-resolved DRIFTS spectra during the modulation and after averaging into one single period are reported in Figure S10.

For LFO (Figure S10a–d), we can see a greater extent in the formation of carbonates in the region 1200–1800 cm^{-1}, as the temperature increased. Additionally, bands are observed above 3000 cm^{-1}, indicative of the O–H stretching mode of bicarbonates and thus their formation, while the gas-phase CO_2 signal near 2350 cm^{-1} is minimal even at the highest temperature. Note that no atmospheric compensation was considered in the data processing, and so, the almost constant CO_2 amount at 150 °C could be due to incomplete purging of the cell from the atmospheric CO_2. This is in line with the low activity of the LFO sample observed in the kinetic studies. For the LFCO (Figure S10e–h), the same types of species are observed with two distinct differences. First, the relative ratio of OH bands vs. the carbonates is decreased significantly, which is consistent with the less acidic nature of LFCO, as confirmed by NH_3-TPD. Second, the formation of the CO_2 signal is promoted at higher temperatures in correlation with the less intense carbonate bands. Note that the highest amount of carbonates correlates with the highest amount of CO_2. Also, during the second half period, when the sample is exposed only to He, the carbonate bands are decreasing, which could be due to the partial thermal decomposition of the carbonates reaching a stable concentration on the surface. This effect is more significant at higher temperatures and when cobalt is present in the sample.

To explore the reaction mechanism, discarding the contribution of non-involved species (*e.g.*, atmospheric CO_2 and H_2O), and participation of carbonates in the reaction paths under steady-state conditions, the time-resolved spectra were transformed into phase-resolved and demodulated at different indices for phase-sensitive detection (PSD). The phase-resolved data at the fundamental modulation frequency (k = *1*) were also used to show the detailed band assignment as discussed in the next sections.

3.3.2. Phase-Resolved DRIFTS Spectra. The phase-resolved spectra at k = *1*, for the two samples and at different temperatures, are shown in Figures S11 (carbonates, CO_2 and CO) and S12 (OH), along with the obtained phase delays. Before getting to the details of the phase analysis, we used the data of the carbonate region for the two temperature extremes (plotted in Figure 2) to identify the different types of carbonates on the two catalysts. Different types of carbonates are classified based on the different coordinations to the surface according to the surface acidity and the cationic sites (Scheme 2), resulting in differing thermal stability. A more in-depth analysis of the different carbonate types in IR spectroscopy is given in the supporting information.

For the LFO sample at 100 °C (Figure 2a), bicarbonate, bidentate, and monodentate carbonate species can be observed (see the SI for more details on the characterization of the carbonate bands). All bands are summarized in Table 2, which displays all the modes identified for all species with their relative frequencies (see the SI for detailed assignments).

By increasing the temperature for LFO, a few differences can be observed (Figure 2b), although the position of the bands remains the same. Interestingly, the bicarbonate species, defined by the bands at 1391 and 1216 cm^{-1}, display a lower relative intensity at a higher temperature than 100 °C in comparison to the other carbonates. At the same time, in the OH region, a stronger modulation of the bands below 3650 cm^{-1} still indicates the presence of bicarbonate species (Figure S12). This may suggest that the bicarbonate species modulate in a similar way in the whole measured temperature range, with their intensity not significantly changing. This causes the low-frequency

https://doi.org/10.1021/acscatal.6c01338
ACS Catal. 2026, 16, 12062–12079

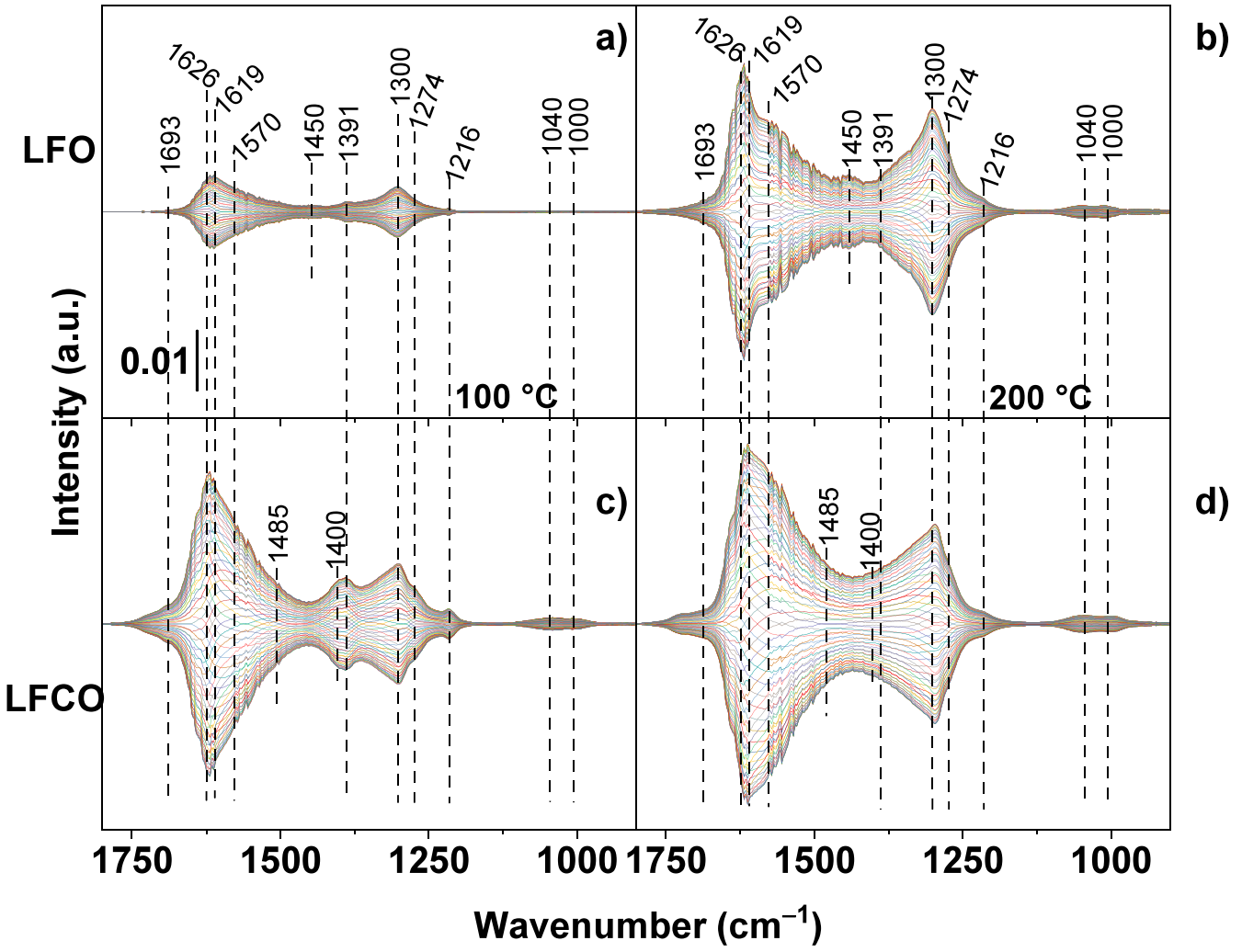

Figure 2. Phase-resolved spectra collected at 100 °C (a) and 200 °C (b) on LFO, and at 100 °C (c) and 200 °C (d) on LFCO samples at demodulation index $k = 1$. The frequencies reported are the same as those reported in Table 2. The intensity of all subplots is the same as shown in panel (a).

Scheme 2. Schematic Representation of Mono- and Bidentate Carbonates, Where *M* Indicates Generic Metallic Sites[51−55]

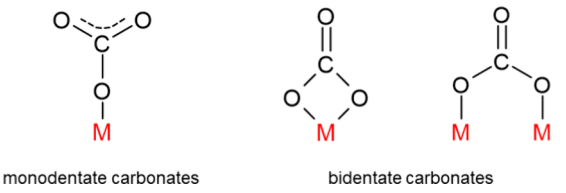

bands of the bicarbonates to be overshadowed by the larger carbonate bands. On the other hand, the bidentate carbonate bands (1619 and 1300 cm^{-1}) have higher intensity, suggesting a higher modulation under MES conditions. These findings indicate that the majority of the monodentate species can be converted to bidentate species at higher temperatures or that such high temperatures facilitate the formation of more bidentate carbonates. A major difference is an additional band at 1570 cm^{-1}, which is more distinguishable as the temperature increases (see Figures S10 as well). This band can be ascribed to a second family of bidentate carbonates generated at higher temperatures and can be related to ν(C=O). While the band related to ν_{asym}(O–C–O) has been ascribed to the shoulder at around 1340 cm^{-1}, which can be barely visible in Figures 2 and S10 for the spectra collected at 200 °C. Since these bands appear when the temperature increases, we assumed that this new family of bidentate carbonates was generated by the conversion of monodentate species.

For LFCO, Figure 2c,d presents a series of spectral bands that can be attributed to the same carbonate species identified in Figure 2a,b. However, all carbonate bands are slightly shifted compared to those of LFO, indicating that the electronic surface properties are changed upon cobalt inclusion. In particular, the acidity of the surface seems to be decreased in line with the NH_3-TPD results. This is highlighted by the presence of more monodentate carbonate species (highlighted by the band at 1400 cm^{-1}), which are more common on basic oxides.[51,52,54] Overall, the modulation of the carbonate bands on LFCO is accompanied by a significant increase in the CO_2 band, especially at higher temperatures (see Figure S11), indicating a

https://doi.org/10.1021/acscatal.6c01338
ACS Catal. 2026, 16, 12062−12079

Table 2. Vibrations and Their Wavenumber (cm^{-1}) for Different Carbonates Formed on the Surface of the LFO and LFCO Catalysts[51−55]

surface species	sample	ν(C=O)	ν(C–OH)	ν(C–OM)	ν_{as}(O–C–O)	ν_{s}(O–C–O)	δ(COH)
m-HCO_3^-(bicarbonate)	LFO	1626	1391				1216
	LFCO	1693	1391				1216
b-$CO_3^=$(bidentate carbonates)	LFO	1619–1570			1300–1250	1013	
	LFCO	1630–1612			1300–1274	1000	
m-CO_3=(monodentate carbonates)	LFO			1050	1450	1312	
	LFCO			1040	1485	1400	

correlation between the carbonate formation/decomposition and the CO_2 formation.

Note that infrared spectroscopy cannot help in distinguishing which species are associated with La^{3+}, Fe^{3+}, or Co^{3+}.[51,52,56] By increasing the temperature, the spectra slightly change (Figure 2d). First, the intensities of all bicarbonate bands (1693, 1391, and 1216 cm^{-1}, Table 2) get relatively lower at higher temperatures (120, 150, and 200 °C) relative to the bands at 100 °C, indicating lower stability of these species on LFCO or a lower likelihood of their formation at high temperatures.

The other remaining bands are related to the same species reported in Figure 2a. However, the monodentate-species components (1485, 1400, and 1040 cm^{-1}, Table 2) at higher temperatures are becoming convoluted (Figure S11). This can be ascribed to different reasons, such as (i) an overlapping of bidentate-species bands; (ii) a conversion of monodentate to bidentate carbonates, (iii) decomposition to CO_2 and desorption during heating. Nonetheless, one event cannot exclude the others, and all of them could have occurred. In light of our findings, considering the spectra collected in both the time and the phase domains, and the larger increase in the intensity of the bidentate carbonate bands, we conclude that both the conversion of monodentates to bidentates and the decomposition to CO_2 are more likely to occur on LFCO.

It is noteworthy that the LFCO catalyst, in particular at 200 °C, also presents some differences in the OH region compared with LFO (see Figure S12 for details). In the LFCO spectra, besides the band centered at 3620 cm^{-1}, two additional features at 3700 and 3725 cm^{-1} can be observed. To the best of our knowledge, it was not possible to definitely assign both the bands at 3700 and 3725 cm^{-1} to specific acidic sites. However, considering their presence on the LFCO sample, we can address their presence as induced by the cobalt inclusion.

For both catalysts, the DRIFTS-MES spectra suggest that the second family of bidentate carbonates (1570 cm^{-1}) prominently observed at 200 °C includes active species because of its high modulation at higher conversions and temperatures. While monodentate carbonates seem to be less stable at higher temperatures, their higher modulation on LFCO than on LFO also shows that they are possibly the species responsible for the low-temperature activity up to 150 °C (Figure S11). Meanwhile, bicarbonates are not readily converted to CO_2 due to their low modulation, which is in good agreement with studies on Pt/Al_2O_3, suggesting hydroxy-carbonates to be inactive and linear and bridged carbonyl-type species to be both active.[19] Due to their modulation, these bicarbonate species are not true spectator species, most likely because of the decomposition of carbonates taking place at this temperature.

3.3.3. Phase Delays at Different Demodulation Indices (*k*). By changing the demodulation index (k) in eq 2, MES-PSD can provide kinetic information and filter out phenomena with different occurrence frequencies.[23,35] As a result, as k increases, the sensitivity to detect short-lived species, *i.e.*, those modulating at faster frequencies, increases accordingly, which improves the detection of transient species.[35,36,38] By means of the in-phase angle analysis (eq 3) performed at different k values and focused on different species, it is possible to investigate the reaction pathway.[35] However, some species are featured by more than one band, as already displayed in Figures 2 and S11. Thus, the indicative unique bands related to the identified species were used to study their behaviors at different k values. In particular, we only chose the bands with the highest intensity that are perfectly isolated from the others to avoid overlapping with other components and are present in almost all the spectra. In this regard, we considered the band related to the δ(CÔH) of bicarbonate species at 1216 cm^{-1}, the bands at 1619 cm^{-1} of the different carbonate species, and the band at 2359 cm^{-1} related to CO_2. Also, considering the trend in the temperature effect, we only focused on the two extremes, namely, 100 and 200 °C. All the phase delays of the abovementioned species are compared in Figure 3.

From the demodulation analysis of LFO at 100 °C (Figure 3a), it is clear that carbonates and bicarbonates are formed almost simultaneously, displaying analogous behavior at different k values. Indeed, their phase delays become more negative at higher demodulation frequencies. Since the phase angles correspond to a specific spectrum at a specific wavenumber with the largest intensity, it is possible to determine a time value from a phase angle as reported in the literature.[57] More specifically, the more negative the phase angle, the larger the time required by a specific species to reach the largest intensity.

Regarding CO and CO_2, their peaks are related to those of the two molecules in the gas phase. In this regard, CO follows an isolated trend, as evidenced by its more negative phase delay compared to that of the carbonates with increasing k. This suggests that CO accumulation in the gas phase is probably slower than the formation of surface carbonates. Indeed, at $k = 1$, the phase delay is actually less negative than that of carbonates, while at $k = 7$, the phase delay is more negative, suggesting a slower rate. A similar situation can be described for CO_2. However, it should be noted that both CO and CO_2 were detected during the accumulation in the gas phase. By using a flow-through mode in the DRIFTS cell, the effect of gas accumulation is minimized, and therefore, the comparison between the phase delays of gas-phase product, *i.e.*, CO_2 and surface species is possible. Nonetheless, especially for CO_2 at $k = 3$ and $k = 5$, there is a random trend in the phase delays at different

https://doi.org/10.1021/acscatal.6c01338
ACS Catal. 2026, 16, 12062−12079

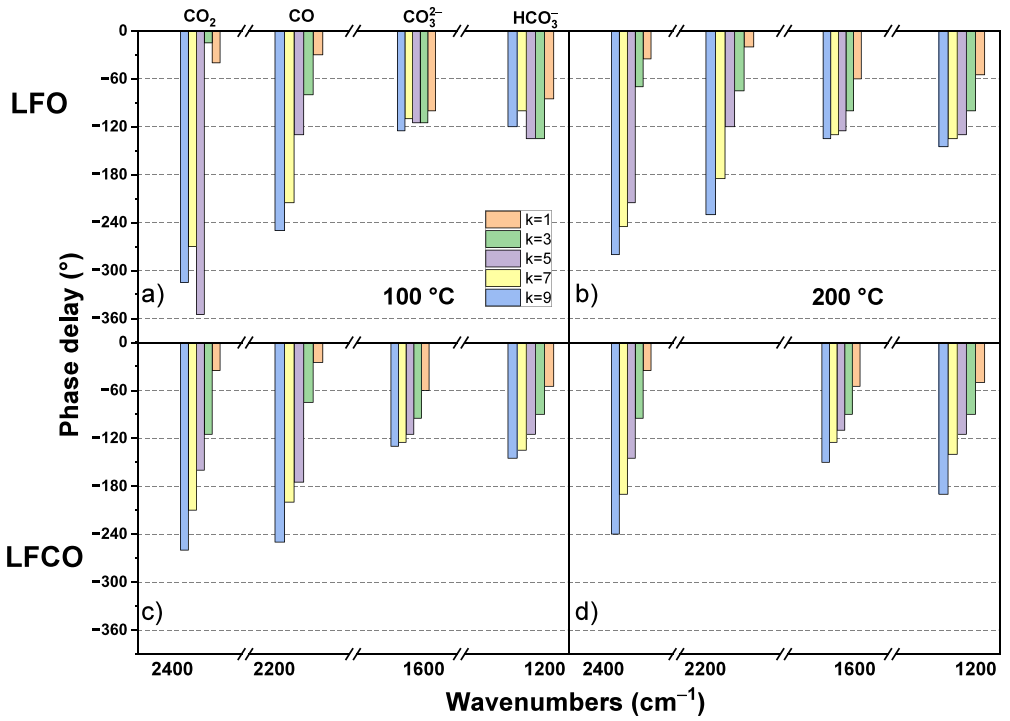

Figure 3. Phase delays of different species after PSD analysis: LFO at 100 °C (a) and 200 °C (c); LFCO at 100 °C (b) and 200 °C (d). (Note: each bar related to each group belongs to the same frequency.)

k values. Therefore, for $k > 1$, we cannot exclude that the intensity of the bands might be below the detection threshold, considering the lower signal-to-noise ratio at higher k indices.

Regarding LFO at higher temperatures (120, 150, and 200 °C, see Figures S11 and 3), the situation is almost unchanged. Carbonates and bicarbonates are formed almost at the same phase and before saturation of the gas phase with CO_2 and CO.

To summarize, CO oxidation on the LFO perovskite catalyst seems to occur by carbonate formation at the catalyst surface first, followed by decomposition to CO_2 and its desorption. This corresponds to the hypothesis of the catalytic tests, suggesting a pure carbonate-mediated MvK mechanism according to pathway B (Scheme 1).

When cobalt ions are present in the perovskite structure, there is a small yet important change in the infrared spectra. Indeed, under steady-state conditions, carbonates and bicarbonates are the first species to be formed and CO_2 is formed after them, as observed for LFO. However, considering the trend of all phase delays, the variation of the phase delays of a single species with increasing k indices is different. More specifically, the phase delays for the carbonate species and CO_2 on LFCO at 100 and 200 °C increase almost linearly with increasing k indices, whereas the phase delays observed for LFO at the same temperature appear to level off for $k > 3$. This can be mainly related to the higher activity of LFCO compared with LFO. Regarding the PSD analysis of LFCO at 200 °C, the variation of the phase delays from $k = 1$ to $k = 9$ can be linked to the persistent formation of some carbonates at these temperatures, as highlighted by the time-domain spectra (Figure S10h). This was not the case for LFO, where the lower catalytic activity leads to a rapid saturation of the surface at both temperatures since the very first instant, leading to a very similar phase delay at almost all k indices. This behavior is demonstrated by the time-domain spectra reported in Figure S10 and by the small variation in the phase delays in the PSD analysis in Figure 3a,c.

In summary, cobalt inclusion positively influences the formation of carbonates, which do not immediately saturate the surface. In view of two competing processes, where the carbonates are first formed on the surface and then decomposed to form CO_2, the cobalt ions seem to increase the decomposition rate of the carbonate species, leading to a lowering of the surface poisoning derived from their saturation, which we hypothesize to be responsible for the decline in the catalytic activity. This would also suggest that this mechanism follows the MvK mechanism according to pathway B. However, no adsorbed CO_2 or O can be observed via DRIFTS-MES, making the analysis of the occurring LH-type mechanism on LFCO not possible with this method. However, the hypothesis of a mechanism following only pathway A can be disproven, and both catalysts follow pathway B with their MvK mechanism. The higher activity is thereby not due to a lower formation of carbonates on LFCO but rather a faster decomposition, as was shown by the PSD analysis.

3.4. DFT + U Calculations

DFT + U calculations were additionally employed to gain insight into the CO oxidation process by simulating the reaction pathways for both LFO (black pathway) and LFCO (pink pathway), as shown in Figure 4. The corresponding cells are displayed in the supporting information (Figure S13). For these calculations, the initial, pristine state of both catalysts was considered. The CO molecule interacts with the oxygen surface atom, resulting in the formation of CO_2 and the creation of an oxygen vacancy on the surface, occurring in four distinct steps as illustrated in Figure 4a. In the initial step, CO and the surface are positioned far from each other, with no

https://doi.org/10.1021/acscatal.6c01338
ACS Catal. 2026, 16, 12062−12079

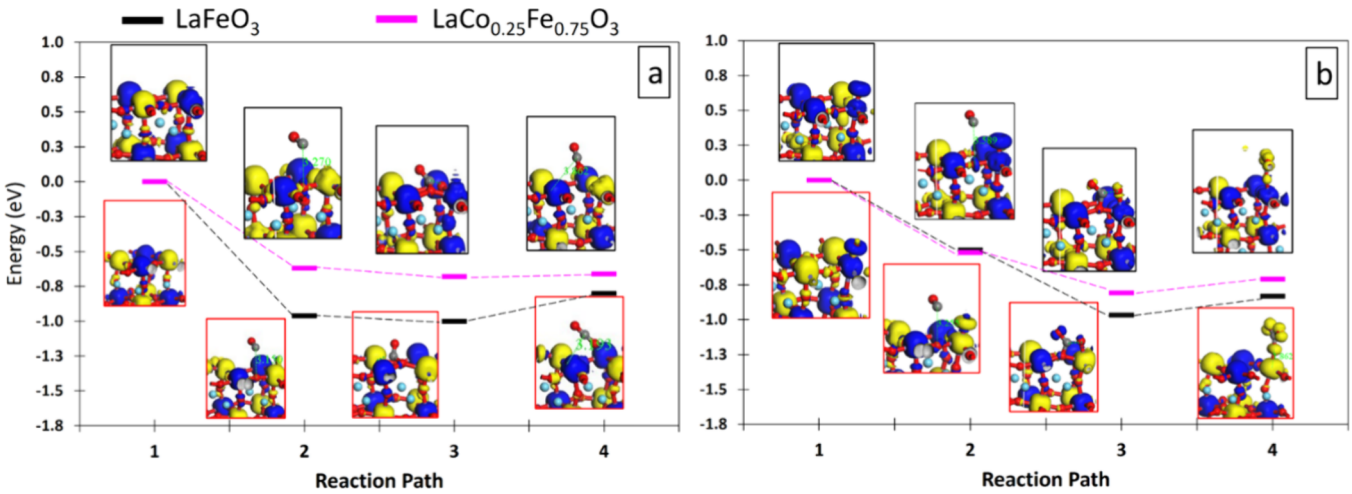

Figure 4. CO oxidation mechanisms for the 0% cobalt (LFO, black) and 25% cobalt (LFCO, pink) samples. (a) Without adsorbed oxygen on the surface. (b) With adsorbed oxygen on the surface. Carbon and oxygen atoms are shown in gray and red, respectively. Yellow and blue represent the majority and minority spin iso-surfaces.

interaction between them, serving as the baseline reference. In step 2, CO relaxes to the vicinity of the surface with a distance of approximately 3 Å. In step 3, CO establishes a bond with the surface, giving rise to the formation of carbonates with a two-bond configuration with two oxygen atoms on the surface. In the last step, CO_2 leaves the surface and one oxygen vacancy forms on the surface. This step is uphill if no cobalt is present, with an energy of around 0.13 eV. In the presence of cobalt, this step is negligible, which can lead to higher activity of this compound for this termination. In Figure 4b, the reaction takes place in the presence of absorbed oxygen on the surface. Our calculations show that a carbonate molecule forms on the surface with two bonds onto the surface and adsorbed oxygen atoms (step 3 in Figure 4b). In the last step (for both 0 and 25% cobalt), carbonate stays on the surface with the single bond to the iron and cobalt atoms. However, both steps are uphill with higher energy steps.

In conclusion, we observed that the interaction of CO and surface oxygen atoms leads to the formation of carbonates with two bonds to the surface oxygen atoms. In the presence of adsorbed oxygen atoms, the reaction involves the formation of carbonates with a single bond to the surface. Since we observed both monodentate and bidentate carbonate species in DRIFTS-MES, a mechanism with and without adsorbed oxygen is possible. However, more monodentate species are observed on LFCO, which could also be related to the mixed MvK- and LH-type mechanism, confirmed by our kinetic measurements, where adsorbed surface oxygen is present. Therefore, adsorbed oxygen on LFCO is possibly present more abundantly during the reaction, even after the pretreatment and deactivation of the catalyst. The energy levels also reveal that CO adsorption is more favorable on LFO without adsorbed oxygen, while on LFO, the energy levels are closer. On LFCO, the final step of carbonate formation is energetically negligible without adsorbed oxygen and slightly endothermic with adsorbed oxygen present. This means, in both cases, according to Scheme 1, the catalyst follows pathway B, a MvK mechanism facilitated by carbonate intermediates, which was already postulated according to our experimental results. It has to be mentioned that the calculations were done on the pristine catalysts. As catalysis and DRIFTS results showed, there are changes via surface deposition and possible reduction of the surface. However, the calculated results show similar trends that we observed in our experiments. We, therefore, propose that additionally, adsorbed oxygen is still present according to our DFT calculations, which was not considered in Scheme 1.

3.5. Operando Spectroscopy NAP-XPS-XANES under Steady-State Conditions

To further disentangle the complexity of the reaction mechanism and the promotional role of cobalt in LFCO catalyst under reaction conditions and help distinguish between the pristine state assumed in DFT + U and the real catalyst state, NAP-XPS-XANES was employed. This technique provides crucial insights into the electronic structure, enabling the understanding of dynamic chemical interactions occurring at both surface and subsurface layers of the LFCO catalyst (5–10 Å) during CO oxidation after O_2 pretreatment at 250 °C (Figures 5 and S14). In addition, this method enables real-time monitoring of catalytic performance alongside the spectroscopic information under steady-state conditions. The recorded conversions of CO and O_2, as well as the CO_2 yield, are stable during the NAP-XPS experiments (Figure S14a). Furthermore, activity can be observed even at 120 °C with 0.2% (Figure S14b). However, the maximum conversion at 250 °C is only 4.5%. The temperature program was also performed under the same conditions as the catalytic measurements. Here, the CO conversion is not stable at higher temperatures, as was already observed during the catalytic experiments (Figures S5, S6b and S14c), and at 250 °C, LFCO reaches 80% conversion, as was also expected from catalysis experiments. These differences are simply due to limitations in the catalyst amount and flow rate of reactive gases. However, the composition ratio of the reactive gases and the temperature were similar to the catalytic measurements, hence keeping the chemical potential as similar as possible.

3.5.1. Carbonates in XPS. Since no experimental molecular reference can faithfully reproduce the chemical, electrostatic, and screening environment of carbonates chemisorbed on a La/Fe/Co-perovskite surface, our peak assignments rely on the

https://doi.org/10.1021/acscatal.6c01338
ACS Catal. 2026, 16, 12062−12079

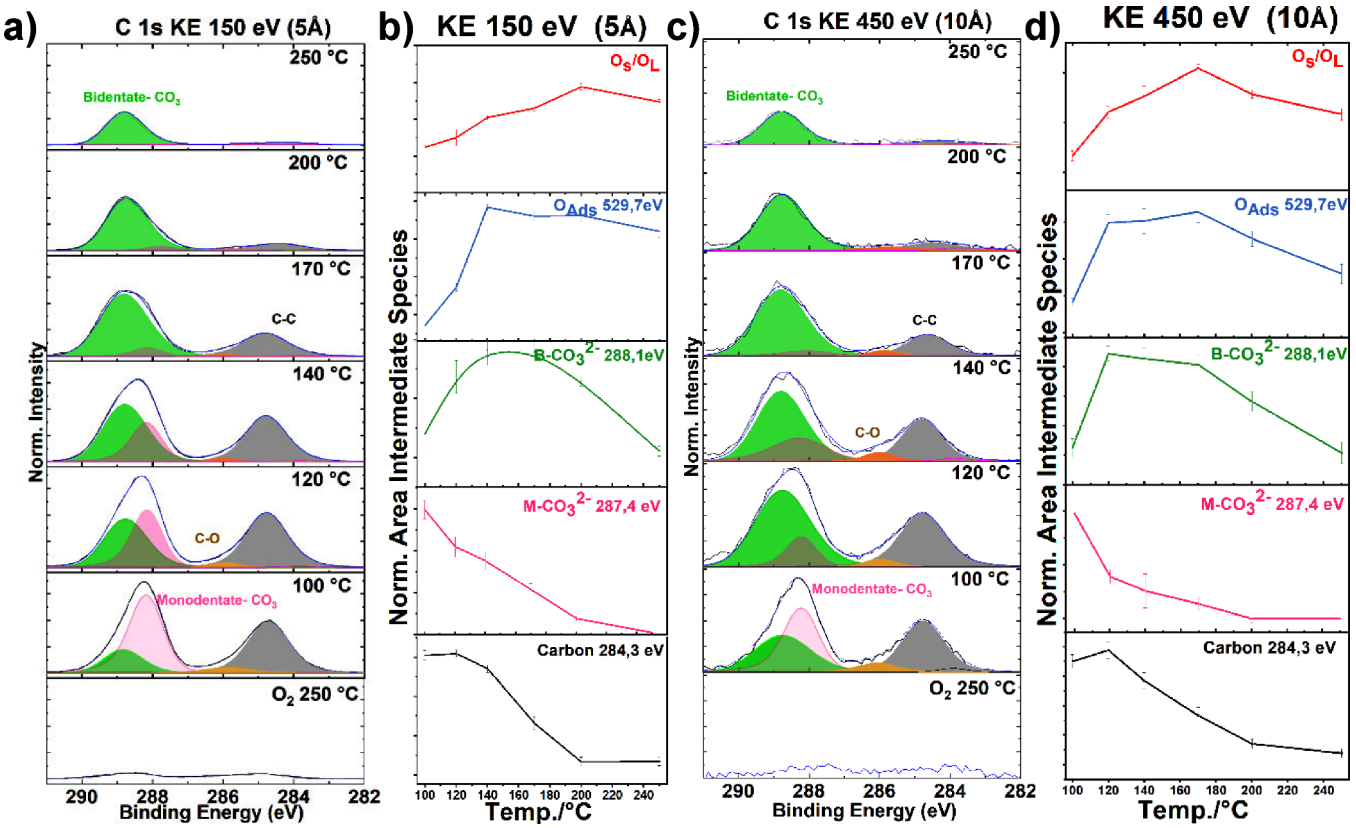

Figure 5. (a–c) Operando NAP-XPS C 1s spectra under CO:O_2 (1:1) 0.25 mbar from 100 °C to 250 °C with KE 150 eV (5 Å) and KE450 eV (8 Å) (b–d) comparison between the normalized spectral areas calculated from C 1s and O 1s (Figure S15). Fitting parameters given in Tables S1 and S2.

first-principles core-level shifts calculated and compared with experimental XPS spectra by Whitten et al.[58] for monodentate and bidentate carbonate configurations on $LaCoO_3$, complemented by the experimental NAP-XPS literature on related La-containing perovskites and cobalt oxides.[59−61] NAP-XPS analysis of the C 1s and O 1s spectra (Figures 5 and S15) revealed oxidized carbon species associated with carbonate formation on LFCO during CO oxidation. Within the framework of mechanistic pathway B, where CO oxidation proceeds via carbonate intermediates, we interpret the spectral evolution in terms of CO_2 chemisorption and subsequent carbonate formation at the perovskite surface. This interpretation is consistent with reports by Tezel et al. and Whitten et al., who showed that CO_2 chemisorption on perovskite oxides (*e.g.*, $LaFeO_3$, $LaCoO_3$) leads to the stabilization of well-defined carbonate configurations. Such carbonate formation has long been recognized as a representative model for CO_2 capture on perovskites, providing a relevant framework for understanding the behavior of LFCO. During CO_2 chemisorption, the electrophilic carbon atom coordinates with lattice oxygen or with adsorbed oxygen species derived from molecular O_2. The C 1s region exhibits a signal corresponding to carbon bound to three oxygens in a carbonate environment[59] with binding energies spanning 287.4−288.8 eV, depending on the coordination geometry.[60] The higher-energy component (∼288.8 eV) is attributed to bidentate carbonates, where electron density is displaced from the central carbon toward the coordinating oxygens, increasing its electropositive character, consistent with the trends reported by Tezel et al.[58,62] In contrast, monodentate carbonates appear at lower binding energies (∼288.2 eV), reflecting stronger direct interaction of the oxygens with surface cations, which reduces charge withdrawal from the central carbon.

The O 1s region further corroborates these assignments. For bidentate carbonates, two distinct oxygen environments are observed: (i) a component at ∼530.9 eV, assigned to oxygens directly coordinated to electropositive cations (Co, Fe, La), which decreases local electron density from oxygen, and (ii) a component at ∼530.6 eV, associated with non-coordinated C=O groups. In contrast, monodentate carbonates exhibit a single peak at ∼530.2 eV, as both non-coordinated oxygens interact symmetrically with the perovskite surface.

These assignments are consistent with the DFT core-level shift calculations of Whitten et al.,[58] which clearly differentiate between monodentate and bidentate carbonate configurations. Importantly, their study demonstrated that CO_2 chemisorption stabilizes carbonate species through either (i) asymmetric binding (bidentate), where one oxygen remains non-coordinated, or (ii) symmetric binding (monodentate), where both oxygens interact with surface cations.

Taken together, the combined NAP-XPS evidence and comparison with theoretical models support a mechanism in which carbonate formation and transformation, governed by coordination geometry and electronic redistribution, play a central role in dictating surface reactivity during CO oxidation over LFCO. These findings are also consistent with the DRIFTS and DFT + *U* findings.

A clear temperature-dependent evolution of these species is observed between 100 and 140 °C (Figure 5). As the

https://doi.org/10.1021/acscatal.6c01338
ACS Catal. 2026, 16, 12062−12079

temperature increases, the C 1s signal at 288.2 eV decreases, while the feature at 288.8 eV becomes more prominent, indicating a progressive surface transition from monodentate to bidentate carbonates, indicating a transformation in the electronic environment of surface-bound carbon species.

Parallel evolution in the O 1s region displays the same two distinct oxygen environments noted above. Specifically, the component associated with monodentate carbonates at 530.2 eV decreases with temperature, while the components associated with bidentate carbonates increase (530.9 eV and 530.6 eV). This trend shows that increasing temperature causes the catalyst surface to shift from monodentate to bidentate carbonate species, as supported by DRIFTS-MES data. These electronic changes modulate surface basicity and reactivity on perovskite oxides, which provide a mechanistic rationale for the temperature-dependent evolution of carbonate species. Monodentate carbonates, enriched in electron density, act as stronger basic sites[63] and display higher reactivity toward CO or CO_2,[64,65] whereas bidentate carbonates, with asymmetrically coordinated oxygens bound to cations, are more stable but exhibit reduced nucleophilicity.[66−69] Also, the observed differences between "surface" (5 Å) and "subsurface" (10 Å) signals for bidentate and monodentate carbonates can be interpreted as depth-sensitive trends in the relative abundance and stability of these adsorbates, rather than proof of true subsurface incorporation (Figure 5). Given that the higher kinetic energy spectra integrate contributions from both the surface and near-surface regions, these "subsurface" trends likely reflect depth-weighted differences in adsorbate populations rather than incorporation of carbonates into the LFCO lattice. The term "subsurface" in our discussion refers to the information depth of NAP-XPS at the higher kinetic energy region, around 10 Å, rather than implying that carbonates are structurally embedded within the lattice. Since the spectra at different photon energies represent integrated signals over their respective sampling depths, the "subsurface" spectra may still contain a significant contribution from surface species, particularly carbonate adsorbates, weighted by their attenuation length.

In line with this picture, NAP-XPS reveals a distinct feature at 286.1 eV (with a corresponding signal at 529.4 eV), assignable to weakly adsorbed C−O species ($CO-Co^{2+}/Fe^{2+}$, $CO-Co^{3+}/Fe^{3+}$). At low temperatures, the higher nucleophilicity and basicity of monodentate carbonates promote dynamic interactions with surface C−O intermediates around 5 Å, enabling their transient stabilization. The weak intensity of C−O indicates that only a minor fraction of surface sites hosts such species, while their progressive attenuation with increasing temperature underscores their role as short-lived intermediates, fully consistent with the proposed reaction pathway. A comparable temperature-dependent decrease is observed for monodentate carbonate species. Between 100 and 170 °C, both monodentate carbonates and weakly adsorbed C−O species are strongly suppressed, suggesting a mechanistic link in which C−O intermediates evolve into monodentate carbonates before ultimately releasing CO. In striking contrast, the O 1s signal at 529.7 eV, attributed to adsorbed oxygen species (O_{ads}), exhibits the opposite temperature trend: while C−O intermediates diminish, the concentration of O_{ads} derived from molecular O_2 increases. This evolution coincides with the catalytic light-off curve and the onset of maximum conversion. The rise in both surface and subsurface in O_{ads} between 100 and 250 °C parallels the emergence of bidentate carbonates.

A C−C signal at 284.8 eV also emerges in the temperature range of 100–140 °C, consistent with carbon formation. Although not detectable by MES-DRIFT or carbon balance at this temperature, this feature is clearly resolved by NAP-XPS, and it is not an artifact of beam-induced deposition. Although the precise origin of this species cannot be fully resolved within the scope of our work, its formation is consistent with carbon generated via CO dissociation at oxygen vacancies, as previously reported for Co_3O_4.[61] Related precedents are found in Fischer−Tropsch catalysis, where CO adsorption on metallic cobalt surfaces facilitates C−C chain growth through partially reduced cobalt centers and Co−O−C motifs.[70] By extension, in our LFCO system, analogous pathways may emerge from partially reduced cobalt sites or Co−O−C surface intermediates stabilized under CO oxidation conditions. The simultaneous appearance of carbonates at these temperatures suggests that CO is still converted to carbonates at other surface sites. While monodentate carbonates are quite active and unstable, as described above, the absence of conversion at these temperatures suggests that they do not decompose, possibly due to carbon deposition blocking active sites and lowering the catalyst's activity.

While the catalyst seems inactive at these temperatures, the above-proposed surface restructuring process aligns with the concept of a frustrated surface phase transition,[32,71] characterized by incomplete surface relaxation arising from competing interactions between CO and O_2 adsorbates and lattice strain. This frustration stabilizes multiple adsorption motifs and increases electronic affinity, facilitating the transition from monodentate to bidentate carbonate species with active carbon participation and decreasing the basicity of the surface. The frustrated surface phase transition, particularly pronounced between 100 and 170 °C, facilitates the coexistence and dynamic reorganization between carbonate species across the surface and subsurface regions. This is supported by the normalized spectral area maxima of bidentate and monodentate carbonate adsorbates (green and pink plots, Figure 5a,c), with bidentates appearing to saturate at lower temperatures in the deeper-probed spectra (120 °C) compared to the surface-sensitive spectra (140 °C) and generally showing higher stability.

As the temperature increases to 170 °C, the deposited carbon is burned off to CO_2. At 200 °C, almost all surface and near-surface carbon is removed. At the same time, the less stable monodentate carbonates also disappear, leaving only bidentate carbonates as intermediates.

The O 1s spectra further resolve the dynamics of two principal oxygen species: exposed surface oxygen at 528.9 eV (O_s) and lattice oxygen at 528.2 eV (O_L).[58] The evolution of the O_s/O_L ratio provides a direct fingerprint of oxygen participation in CO oxidation. With increasing temperature, the O_s/O_L ratio rises and reaches a maximum around 200 °C, after which it stabilizes. This trend indicates that oxygen from the perovskite lattice is progressively activated and replenishes the surface reservoir, thereby sustaining the catalytic cycle. The transient increase of O_s relative to O_L suggests enhanced oxygen exchange across the gas−solid interface, where lattice oxygen is mobilized to the surface and converted into reactive O_{ads} species. Such dynamics are consistent with a Mars−van Krevelen mechanism, in which lattice oxygen participates directly in CO oxidation while molecular O_2 restores the lattice through reoxidation. The stabilization of the O_s/O_L ratio at higher

https://doi.org/10.1021/acscatal.6c01338
ACS Catal. 2026, 16, 12062−12079

temperatures reflects the establishment of a steady-state balance between oxygen consumption and replenishment, coinciding with the light-off curve and maximum catalytic conversion.

Together, these findings outline a temperature-driven mechanism for CO oxidation over LFCO: at 100–140 °C, CO disproportionation and LH pathways dominate, generating a frustrated surface phase transition involving carbon and carbonate species that inhibit further reactivity. As the temperature rises to 170–250 °C, the frustrated phase collapses, surface basicity decreases, and MvK enables conversion of monodentate to bidentate carbonates followed by their decomposition, enhancing catalytic activity and CO_2 evolution. The mechanistic complexity underscores the dynamic nature of the LFCO surface and the pivotal role of evolving carbonate species within the frustrated phase in dictating the reaction pathway.

The spectra for LFO are described in the SI (Figure S23). As was observed on the ME-DRIFTS, the same species could be observed as on LFCO; however, less monodentate is formed at low temperatures. Additionally, the monodentate species are observed at all temperatures, even at 250 °C, highlighting the slower decomposition rate of carbonates on LFO previously described.

3.5.2. Oxidation States in XPS/XANES. The evolution of cobalt and iron oxidation states during CO oxidation was monitored by NAP-XPS (Figure 6a–d) in both the surface and subsurface. A partial reduction of Co^{3+} (779.5 eV, satellite at 789.5 eV) to Co^{2+} (780 eV, satellite at 786.5 eV)[72] was observed. The normalized Co^{2+}/Co^{3+} area ratio spiked at 120 °C (see Figure S17, reporting Co L_3-edge XANES), coinciding with the emergence of the frustrated surface phase transition, where surface reorganization and carbonate transformation from monodentate to bidentate occur. After the initial spike (100–170 °C), the Co^{2+}/Co^{3+} ratio decreases again and stabilizes between 200 and 250 °C at a slightly higher value than the initial state at 100 °C. This indicates the gradual relaxation of the frustrated-phase transition and the onset of catalytic activity. At 250 °C, the surface cobalt is further reduced to a similar ratio as was seen at 100 °C, while the subsurface follows the same steady behavior. This behavior indicates that cobalt actively participates in CO oxidation at the surface, with Co^{3+} acting as an electron acceptor from CO to facilitate CO_2 and carbonate formation.

Iron spectra (Figure S16), in contrast, exhibited a slight increase in Fe^{3+} (710.0 eV, satellite at 719.5 eV) relative to Fe^{2+} (708.3 eV, satellite at 713.7 eV),[72,73] with minor changes in the Fe^{2+}/Fe^{3+} normalized area ratio between 100 °C and 140 °C. This suggests that Fe^{3+} formation partially compensates for Co^{3+} reduction, helping to maintain charge neutrality in the perovskite during the restructuring associated with the frustrated-phase transition. After 140 °C, the iron oxidation state remains relatively constant, supporting the notion that the major redox reorganization is confined to the temperature window where the frustrated-phase transition is dominant.

In contrast, Fe L_3-edge XANES (Figure S18) spectra show two main contributions, associated with Fe^{2+} at 708.3 eV and Fe^{3+} at 710.2 eV.[74] Unlike cobalt, the iron oxidation state distribution is similar in both AEY and TEY signals, indicating a homogeneous Fe^{3+}-rich environment throughout the perovskite structure. The normalized Fe^{2+}/Fe^{3+} intensity L_3 edge ratio exhibits a slight decrease in Fe^{2+} content between 100 °C and 140 °C, stabilizing at higher temperatures. This behavior reflects the greater redox stability of iron under reaction conditions and is consistent with trends observed in NAP-XPS measurements.

The distinct redox behaviors of cobalt and iron, as revealed by complementary NAP-XPS and XANES analyses, are closely linked to the evolution of the frustrated surface phase transition during CO oxidation. Within the frustrated-phase regime (100–170 °C), the enhanced reducibility of cobalt leads to significant Co^{2+} accumulation, which stabilizes monodentate and bidentate carbonate species through Lewis acid–base interactions. This restructuring is a hallmark of the frustrated state, characterized by incomplete surface relaxation, dynamic competition among adsorbates, and evolving oxygen lattice changes. As the temperature increases beyond 170 °C and the frustrated phase progressively collapses, Co^{3+} regeneration becomes favored, accompanying the decomposition of accumulated carbonates and triggering a sharp rise in CO_2 production. In contrast, iron displays minimal changes in oxidation state during this transition, underscoring its role in stabilizing the perovskite framework throughout the redox-driven surface reorganization.

The observed differences in redox flexibility between cobalt and iron can be rationalized by their distinct carbonate affinities and electronic structures. Iron exhibits a higher redox potential and higher polarizability compared with cobalt,[75−78] which promotes more facile electron transfer and weaker Co−O bonding, enhancing its susceptibility to oxygen lattice changes, which is a key feature sustaining the frustrated surface phase transition. Consequently, cobalt carbonates are less stable and decompose more readily at elevated temperatures, allowing Co^{2+} species to revert to the oxidized Co^{3+} state on the surface. This behavior aligns with the observed decline in Co^{2+} content beyond 200 °C and the reactivation of catalytic sites.

In contrast, iron forms more stable carbonate species that persist to higher temperatures, resulting in relatively minor changes in its oxidation state across the reaction conditions. This fundamental difference influences the overall oxygen dynamics within the perovskite structure: Co^{3+}, through its lower redox[77] flexibility in comparison with Fe^{3+} during the frustrated-phase transition and higher lattice oxygen change propensity, likely plays a more dominant role in facilitating oxygen mobility compared to iron. The lower redox flexibility was also observed on LFO, where iron emulates the behavior of cobalt in LFCO but to a far lesser degree (see Figures S20 and S21 and the extended discussion in the SI). Such enhanced oxygen transport, enabled by cobalt, provides a plausible explanation for the superior catalytic activity observed in LFCO relative to cobalt-free systems such as LFO. The interplay between B-site redox dynamics and frustrated phase evolution plays a pivotal role in determining catalytic behavior. In this regard, the interplay between the carbonate affinities of iron and cobalt on the perovskite surface offers a pathway to fine-tune catalytic performance. Cobalt actively drives the restructuring and redox cycling necessary for high catalytic turnover, while iron contributes structural robustness.

Additionally, the role of A-site cation (lanthanum) was further examined from the La 3d core-level spectra (see Figure S19 and the following discussion in the SI). As detailed in the SI, lanthanum fulfills a dual role in the frustrated-phase transition: chemically, by stabilizing carbonate intermediates through strong Lewis acid−base interactions, and structurally, by anchoring oxygen lattice changes and enabling the dynamic redox flexibility of the perovskite system. The synergistic interaction between La^{3+} sites and the redox-active B-site cations

https://doi.org/10.1021/acscatal.6c01338
ACS Catal. 2026, 16, 12062−12079

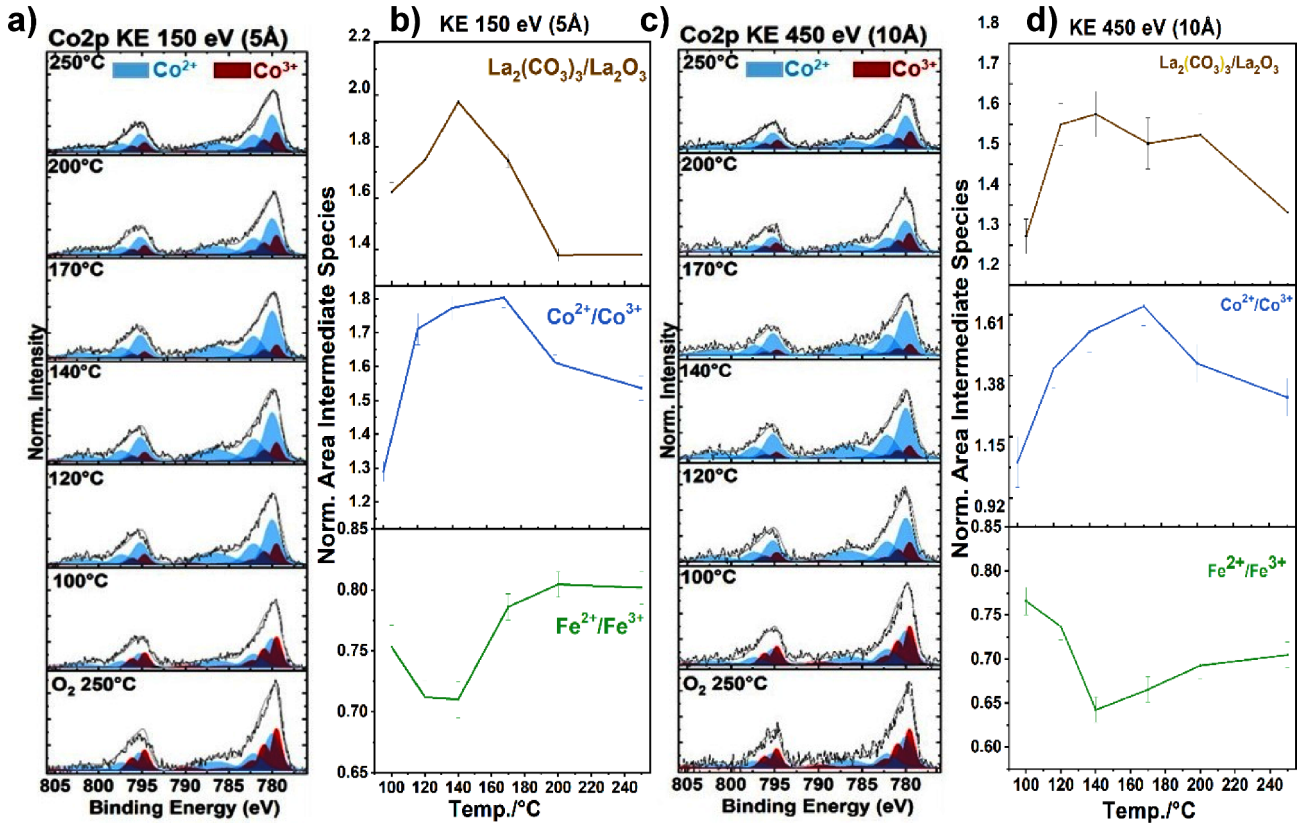

Figure 6. (a–c) Operando NAP-XPS Co 2p spectra of LFCO under CO:O_2 (1:1) 0.25 mbar from 100 °C to 250 °C with KE 150 eV (5 Å) and KE450 eV (8 Å). (b–d) Comparison between the normalized spectral areas calculated from the oxidation states ratio of Co 2p, Fe 2p (Figure S16), and La 3d (Figure S19). Fitting parameters given in Table S5.

(Co^{3+} and Fe^{3+}) proves critical for controlling the evolution of the frustrated surface phase and optimizing catalytic performance during CO oxidation. Without cobalt in the system, *i.e.*, in LFO, the anchoring of carbonates on lanthanum is stronger at low and high temperatures, and the carbonates are more abundant, showcasing the importance of the redox-active partner, especially regarding the more stable bidentate carbonates (see Figures S22 and S23).

4. CONCLUSIONS

In this work, we investigated CO oxidation over the perovskites $LaFeO_3$ (LFO) and $LaFe_{0.75}Co_{0.25}O_3$ (LFCO), reperesenting inactive and active catalysts, respectively. Advanced operando techniques were employed to disentangle the parallel convoluted surface phenomena that are responsible for the reaction progressing on the surface with respect to the concept of the frustrated-phase transition. Special attention was given to the role of the carbonates as the reaction intermediates, as well as the structural transformation on the surface of the catalysts at different reaction conditions, to elucidate the overall reaction mechanism. LFO displayed low activity but high stability under the tested conditions during CO oxidation. A pure MvK mechanism was identified via kinetic studies and confirmed by theoretical calculations. However, the reaction showed a high complexity due to a carbonate-mediated mechanism over mainly bidentate carbonates according to our DRIFTS-MES-PSD analysis. Iron in LFO was identified as the weaker redox active site, which only showed small changes in its oxidation state.

LFCO, on the other hand, displayed higher conversions and a slight deactivation during time on stream. Even with ongoing deactivation, it stayed more active than LFO. The reaction mechanism was also more complex, displaying an interplay between MvK and LH. While similar carbonates were also observed on the cobalt-substituted catalyst, low-temperature monodentate species were found and identified as possible active intermediates via DRIFTS-MES and NAP-XPS. Regardless of the species, LFCO facilitates a faster conversion of the carbonates to CO_2, presumably due to the availability of surface oxygen and not only a pure MvK-type mechanism. The interplay between the reactions was also proven to be temperature-dependent: The LH mechanism is more prominent at lower temperatures, while at high temperatures, the MvK mechanism dominates. For the pristine surface, DFT calculations also confirmed that the presence of cobalt reduces the energy barrier for certain reaction steps, suggesting that LFCO exhibits higher catalytic activity compared to LFO. This trait is inherited by the frustrated-phase transition. In particular, cobalt helps facilitate the release of CO_2, making the reaction more efficient. Additionally, the results indicate that surface-adsorbed oxygen likely remains active during the process, even after catalyst treatment and partial deactivation.

This mechanism shift was also confirmed by NAP-XPS, showing the relative stability of bidentate vs. monodentate ones at temperatures above 170 °C on the LFCO surface and in the sub-surface region. This restructuring was accompanied by a reduction of Co^{3+} and an oxidation of Fe^{2+}. The emerging

https://doi.org/10.1021/acscatal.6c01338
ACS Catal. 2026, 16, 12062−12079

frustrated surface phase transition could be instrumental in the formation of active carbonates as reaction intermediates, which facilitated the reaction at higher temperatures.

While it was shown that especially cobalt plays a role as the active site, iron and lanthanum contribute to the reaction mechanism. La^{3+} stabilizes the perovskite structure due to its ability to compensate for oxygen defects and to stabilize carbonates on the surface. Lanthanum also formed carbonates; however, La-associated carbonates were decomposed differently when cobalt was present, showcasing the synergy between lanthanum and B-site cations. Iron also forms carbonate species while keeping the charge balance of the system in line due to oxidation. While this work focuses on the CO-to-CO_2 reaction, it still highlights a methodology for disentangling the complexity of the reaction mechanism, especially when multiple sites are involved in oxide catalysts used in oxidation reactions.

■ ASSOCIATED CONTENT

Supporting Information

The Supporting Information is available free of charge at https://pubs.acs.org/doi/10.1021/acscatal.6c01338.

Description of the catalytic set-up; XPS fitting parameters; catalyst characterization (PXRD, SEM, BET, NH_3- TPD and RAMAN); catalytic stability, regeneration, repetition, and raw data of temperature and concentration variation; DRIFTS spectra of the time domain, additional temperatures of the phase domain of OH and carbonate regions; mass spectrometry of NAP-XPS-XANES and DRIFTS-MES: NAP-XPS-XANES O 1s, Fe 2p, La 3d (including discussion) and Co and Fe L edge spectra; and unit cells calculated via DFT (PDF)

■ AUTHOR INFORMATION

Corresponding Author

Sharif Najafishirtari – *Institute of Inorganic Chemistry, Christian-Albrechts-Universität zu Kiel, Max-Eyth-Straße 2, Kiel D-24118, Germany; Kiel Nano, Surface and Interface Science KiNSIS, Christian-Albrechts-Universität zu Kiel, Christian-Albrechts-Platz 4, Kiel 24118, Germany;* orcid.org/0000-0003-2121-7439; Email: snajafi@ac.uni-kiel.de

Authors

Nicolas Cosanne – *Institute of Inorganic Chemistry, Christian-Albrechts-Universität zu Kiel, Max-Eyth-Straße 2, Kiel D-24118, Germany*

Daniel Cruz – *Department of Inorganic Chemistry, Fritz-Haber-Institut der Max-Planck-Gesellschaft, Faradayweg 4-6, Berlin D-14195, Germany*

Pierfrancesco Ticali – *Institute of Inorganic Chemistry, Christian-Albrechts-Universität zu Kiel, Max-Eyth-Straße 2, Kiel D-24118, Germany;* orcid.org/0000-0003-3514-0196

Hamidreza Hajiyani – *Institute of Inorganic Chemistry, Christian-Albrechts-Universität zu Kiel, Max-Eyth-Straße 2, Kiel D-24118, Germany; Henkel, AID/Digital Twins & Data Analytics, Düsseldorf 40589, Germany*

Shilong Chen – *Institute of Inorganic Chemistry, Christian-Albrechts-Universität zu Kiel, Max-Eyth-Straße 2, Kiel D-24118, Germany;* orcid.org/0000-0002-2889-403X

Patrick Zeller – *Department of Inorganic Chemistry, Fritz-Haber-Institut der Max-Planck-Gesellschaft, Faradayweg 4-6, Berlin D-14195, Germany; Helmholtz-Zentrum Berlin für Materialien und Energie, Albert-Einstein Straße 15, Berlin 12489, Germany*

Thomas Götsch – *Department of Inorganic Chemistry, Fritz-Haber-Institut der Max-Planck-Gesellschaft, Faradayweg 4-6, Berlin D-14195, Germany;* orcid.org/0000-0003-3673-317X

Alexander Klyushin – *Department of Inorganic Chemistry, Fritz-Haber-Institut der Max-Planck-Gesellschaft, Faradayweg 4-6, Berlin D-14195, Germany;* orcid.org/0000-0003-1305-6911

Axel Knop-Gericke – *Department of Inorganic Chemistry, Fritz-Haber-Institut der Max-Planck-Gesellschaft, Faradayweg 4-6, Berlin D-14195, Germany; Department of Heterogeneous Reactions, Max-Planck-Institut für Chemische Energiekonversion, Stiftstraße 34-36, Mülheim 45470, Germany*

Martin Muhler – *Laboratory of Industrial Chemistry, Ruhr University Bochum, Universitätsstraße 150, Bochum 44801, Germany;* orcid.org/0000-0001-5343-6922

Beatriz Roldan Cuenya – *Department of Interface Science, Fritz-Haber-Institut der Max-Planck-Gesellschaft, Faradayweg 4-6, Berlin D-14195, Germany*

Robert Schlögl – *Department of Interface Science, Fritz-Haber-Institut der Max-Planck-Gesellschaft, Faradayweg 4-6, Berlin D-14195, Germany*

Malte Behrens – *Institute of Inorganic Chemistry, Christian-Albrechts-Universität zu Kiel, Max-Eyth-Straße 2, Kiel D-24118, Germany; Kiel Nano, Surface and Interface Science KiNSIS, Christian-Albrechts-Universität zu Kiel, Christian-Albrechts-Platz 4, Kiel 24118, Germany;* orcid.org/0000-0003-3407-5011

Complete contact information is available at: https://pubs.acs.org/doi/10.1021/acscatal.6c01338

Author Contributions

‡N.C. and D.C. contributed equally. The manuscript was written through the contributions of all authors. All authors have given approval to the final version of the manuscript.

Notes

The authors declare no competing financial interest.

■ ACKNOWLEDGMENTS

This work was funded by the Deutsche Forschungsgemeinschaft (DFG, German Research Foundation)—388390466—TRR 247 within the projects A04, A07, A08, B06, and C01. We thank the Helmholtz-Zentrum Berlin für Materialien und Energie for the allocation of synchrotron radiation beamtime. D.C., T.G., and B.R.C. additionally acknowledge funding by the Federal Ministry of

https://doi.org/10.1021/acscatal.6c01338
ACS Catal. 2026, 16, 12062−12079

Education and Research in the framework of the project Catlab (03EW0015A).

■ ABBREVIATIONS

LFO	$LaFeO_3$
LFCO	$LaFe_{0.75}Co_{0.25}O_3$
MES	modulation-excitation spectroscopy
PSD	phase-sensitive detection
NAP-XPS	near-ambient pressure X-ray photoelectron spectroscopy
MvK	Mars–van Krevelen
LH	Langmuir–Hinshelwood
DRIFTS	diffuse reflectance infrared Fourier transform spectroscopy
PXRD	powder X-ray diffraction
ICP-OES	ion-coupled plasma optical emission spectroscopy
BET	N_2-physisorption after Brunauer, Emmett and Teller
NH_3-TPD	NH_3 temperature-programmed desorption
SEM	scanning electron microscopy
DFT+U	density functional theory
MS	mass spectrometry
XANES	X-ray absorption near edge spectroscopy
Scc	standard cubic centimeters
Ncc	normal cubic centimeters
AEY	Auger electron yield
TEY	total electron yield
E_a	activation energies

■ REFERENCES

(1) Kim, H. Y.; Lee, H. M.; Henkelman, G. CO Oxidation Mechanism on CeO_2-Supported Au Nanoparticles. *J. Am. Chem. Soc.* **2012**, *134* (3), 1560–1570.

(2) Min, B. K.; Alemozafar, A. R.; Pinnaduwage, D.; Deng, X.; Friend, C. M. Efficient CO Oxidation at Low Temperature on Au(111). *J. Phys. Chem. B* **2006**, *110* (40), 19833–19838.

(3) Qu, Z.; Cheng, M.; Huang, W.; Bao, X. Formation of Subsurface Oxygen Species and Its High Activity toward CO Oxidation over Silver Catalysts. *J. Catal.* **2005**, *229* (2), 446–458.

(4) Allian, A. D.; Takanabe, K.; Fujdala, K. L.; Hao, X.; Truex, T. J.; Cai, J.; Buda, C.; Neurock, M.; Iglesia, E. Chemisorption of CO and Mechanism of CO Oxidation on Supported Platinum Nanoclusters. *J. Am. Chem. Soc.* **2011**, *133* (12), 4498–4517.

(5) Wu, C. H.; Liu, C.; Su, D.; Xin, H. L.; Fang, H.-T.; Eren, B.; Zhang, S.; Murray, C. B.; Salmeron, M. B. Bimetallic Synergy in Cobalt−Palladium Nanocatalysts for CO Oxidation. *Nat. Catal.* **2019**, *2* (1), 78–85.

(6) Huang, T.-J.; Tsai, D.-H. CO Oxidation Behavior of Copper and Copper Oxides. *Catal. Lett.* **2003**, *87* (3), 173–178.

(7) Dreyer, M.; Krebs, M.; Najafishirtari, S.; Rabe, A.; Friedel Ortega, K.; Behrens, M. The Effect of Co Incorporation on the CO Oxidation Activity of $LaFe_{1-x}Co_xO_3$ Perovskites. *Catalysts* **2021**, *11* (5), 550.

(8) Dubey, A.; Reddy, K. P.; Gopinath, C. S. Ambient CO Oxidation on In-Situ Generated Co_3O_4 Spinel Surfaces with Random Morphology. *ChemistrySelect* **2017**, *2* (1), 533–536.

(9) Dey, S.; Dhal, G. C. Catalytic Conversion of Carbon Monoxide into Carbon Dioxide over Spinel Catalysts: An Overview. *Mater. Sci. Energy Technol.* **2019**, *2* (3), 575–588.

(10) Freund, H.-J.; Meijer, G.; Scheffler, M.; Schlögl, R.; Wolf, M. CO Oxidation as a Prototypical Reaction for Heterogeneous Processes. *Angew. Chem., Int. Ed.* **2011**, *50* (43), 10064–10094.

(11) Liu, B.; Li, W.; Song, W.; Liu, J. Carbonate-Mediated Mars−van Krevelen Mechanism for CO Oxidation on Cobalt-Doped Ceria Catalysts: Facet-Dependence and Coordination-Dependence. *Phys. Chem. Chem. Phys.* **2018**, *20* (23), 16045–16059.

(12) Cui, X.; Liu, J.; Yan, X.; Yang, Y.; Xiong, B. Exploring Reaction Mechanism of CO Oxidation over $SrCoO_3$ Catalyst: A DFT Study. *Appl. Surf. Sci.* **2021**, *570*, No. 151234.

(13) Chen, S.; Cheng, H.; Liu, Y.; Sun, Q.; Lu, X.; Li, S. CO Oxidation Mechanism on Surfaces of B-Site Doped $SrFeO_{3-\delta}$-Based Perovskite Materials for Thermochemical Water Splitting. *Comput. Theor. Chem.* **2023**, *1224*, No. 114109.

(14) Yu, X.; Zhang, X.; Jin, L.; Feng, G. CO Adsorption, Oxidation and Carbonate Formation Mechanisms on Fe_3O_4 Surfaces. *Phys. Chem. Chem. Phys.* **2017**, *19* (26), 17287–17299.

(15) Cha, X.; He, J.; Fu, Y.; Jiang, B.; Ali, S.; Chen, S.; Zhan, G. Carbonate-Mediated Mars-van Krevelen Mechanism on Cu_xO/CeO_2 Catalysts for Boosting CO Oxidation. *Chem. Eng. J.* **2024**, *501*, No. 157643.

(16) Kim, H. Y.; Han, S. S.; Ryu, J. H.; Lee, H. M. Balance in Adsorption Energy of Reactants Steers CO Oxidation Mechanism of Ag13 and Ag12Pd1 Nanoparticles: Association Mechanism versus Carbonate-Mediated Mechanism. *J. Phys. Chem. C* **2010**, *114* (7), 3156–3160.

(17) Newton, M. A.; Ferri, D.; Smolentsev, G.; Marchionni, V.; Nachtegaal, M. Room-Temperature Carbon Monoxide Oxidation by Oxygen over Pt/Al_2O_3 Mediated by Reactive Platinum Carbonates. *Nat. Commun.* **2015**, *6* (1), No. 8675.

(18) Newton, M. A.; Ferri, D.; Smolentsev, G.; Marchionni, V.; Nachtegaal, M. Kinetic Studies of the Pt Carbonate-Mediated, Room-Temperature Oxidation of Carbon Monoxide by Oxygen over Pt/Al_2O_3 Using Combined, Time-Resolved XAFS, DRIFTS, and Mass Spectrometry. *J. Am. Chem. Soc.* **2016**, *138* (42), 13930–13940.

(19) Hatoum, I.; Bouchoul, N.; Richard, M.; Dujardin, C. Revealing Origin of Hydrogen-Carbonate Species in CO Oxidation Over Pt/Al_2O_3: A SSITKA-IR Study. *Top. Catal.* **2022**, *66*, 915–921.

(20) Peden, C. H. F.; Houston, J. E. Evidence for a Carbonate Species during CO Oxidation on Deactivated Rh(111). *J. Catal.* **1991**, *128* (2), 405–414.

(21) Armaroli, T.; Bécue, T.; Gautier, S. Diffuse Reflection Infrared Spectroscopy (Drifts): Application to the in Situ Analysis of Catalysts. *Oil Gas Sci. Technol. Rev. IFP* **2004**, *59* (2), 215–237.

(22) Mitchell, M. B. Fundamentals and Applications of Diffuse Reflectance Infrared Fourier Transform (DRIFT) Spectroscopy. In Structure-Property Relations in Polymers. In *Advances in Chemistry*; American Chemical Society, **1993**; Vol. 236, pp 351−375.

(23) Urakawa, A.; Bürgi, T.; Baiker, A. Sensitivity Enhancement and Dynamic Behavior Analysis by Modulation Excitation Spectroscopy: Principle and Application in Heterogeneous Catalysis. *Chem. Eng. Sci.* **2008**, *63* (20), 4902–4909.

(24) Holmen, A.; Yang, J.; Chen, D.Steady-State Isotopic Transient Kinetic Analysis (SSITKA)In *Springer Handbook of Advanced Catalyst Characterization*; Wachs, I. E., Bañares, M. A., Eds.; Springer International Publishing: Cham, **2023**, pp 935–965.

(25) El-Roz, M.; Bazin, P.; Daturi, M.; Thibault-Starzyk, F. Operando Infrared (IR) Coupled to Steady-State Isotopic Transient Kinetic Analysis (SSITKA) for Photocatalysis: Reactivity and Mechanistic Studies. *ACS Catal.* **2013**, *3* (12), 2790–2798.

(26) Pansare, S. S.; Sirijaruphan, A.; Goodwin, J. G. Au-Catalyzed Selective Oxidation of CO: A Steady-State Isotopic Transient Kinetic Study. *J. Catal.* **2005**, *234* (1), 151–160.

(27) Dreyer, M.; Cruz, D.; Hagemann, U.; Zeller, P.; Heidelmann, M.; Salamon, S.; Landers, J.; Rabe, A.; Ortega, K. F.; Najafishirtari, S.; Wende, H.; Hartmann, N.; Knop-Gericke, A.; Schlögl, R.; Behrens, M. The Effect of Water on the 2-Propanol Oxidation Activity of Co-Substituted $LaFe_{1-x}Co_xO_3$ Perovskites. *Chem. Eur. J.* **2021**, *27* (68), 17127–17144.

(28) Schlögl, R. Catalysis 40. *ChemCatChem* **2017**, *9* (4), 533–541.

(29) Bartholomew, C. H. Mechanisms of Catalyst Deactivation. *Appl. Catal. A Gen.* **2001**, *212* (1), 17–60.

https://doi.org/10.1021/acscatal.6c01338
ACS Catal. 2026, 16, 12062−12079

(30) Argyle, M. D.; Bartholomew, C. H. Heterogeneous Catalyst Deactivation and Regeneration: A Review. *Catalysts* **2015**, *5* (1), 145–269.
(31) Forzatti, P.; Lietti, L. Catalyst Deactivation. *Catal. Today* **1999**, *52* (2), 165–181.
(32) Schlögl, R. Heterogeneous Catalysis. *Angew. Chem., Int. Ed.* **2015**, *54* (11), 3465–3520.
(33) Sandoval-Diaz, L.; Götsch, T.; Cruz, D.; Vuijk, M.; Lombardi, J. M.; Pietsch, M.; Dembélé, K.; Hammud, A.; Reuter, K.; Scheurer, C.; Knop-Gericke, A.; Lunkenbein, T. Stabilizing Frustrated Phase Transitions in Selective Oxidation Reactions. *Adv. Mater.* **2026**, *38* (8), No. e15292.
(34) Baurecht, D.; Porth, I.; Fringeli, U. P. A New Method of Phase Sensitive Detection in Modulation Spectroscopy Applied to Temperature Induced Folding and Unfolding of RNase A. *Vib. Spectrosc.* **2002**, *30* (1), 85–92.
(35) Urakawa, A.; Ferri, D.; Nuguid, R. J. G.Modulation Excitation Spectroscopy (MES)In *Springer Handbooks*; Springer International Publishing, **2023**, pp 967–977.
(36) Marchionni, V.; Ferri, D.; Kröcher, O.; Wokaun, A. Increasing the Sensitivity to Short-Lived Species in a Modulated Excitation Experiment. *Anal. Chem.* **2017**, *89* (11), 5801–5809.
(37) Marchionni, V.; Newton, M. A.; Kambolis, A.; Matam, S. K.; Weidenkaff, A.; Ferri, D. A Modulated Excitation ED-EXAFS/DRIFTS Study of Hydrothermal Ageing of Rh/Al_2O_3. *Catal. Today* **2014**, *229*, 80–87.
(38) Urakawa, A.; Bürgi, T.; Baiker, A. Kinetic Analysis Using Square-Wave Stimulation in Modulation Excitation Spectroscopy: Mixing Property of a Flow-through PM-IRRAS Cell. *Chem. Phys.* **2006**, *324* (2), 653–658.
(39) Knop-Gericke, A.; Kleimenov, E.; Hävecker, M.; Blume, R.; Teschner, D.; Zafeiratos, S.; Schlögl, R.; Bukhtiyarov, V. I.; Kaichev, V. V.; Prosvirin, I. P.; Nizovskii, A. I.; Bluhm, H.; Barinov, A.; Dudin, P.; Kiskinova, M.Chapter 4 X-Ray Photoelectron Spectroscopy for Investigation of Heterogeneous Catalytic Processes. In *Adv. Catal.*, Academic Press, **2009**, Vol. 52; pp 213–272.
(40) Knop-Gericke, A.; Pfeifer, V.; Velasco-Velez, J.-J.; Jones, T.; Arrigo, R.; Hävecker, M.; Schlögl, R. In Situ X-Ray Photoelectron Spectroscopy of Electrochemically Active Solid-Gas and Solid-Liquid Interfaces. *J. Electron. Spectrosc. Relat. Phenom.* **2017**, *221*, 10–17.
(41) Ravel, B.; Newville, M. ATHENA, ARTEMIS, HEPHAESTUS: Data Analysis for X-Ray Absorption Spectroscopy Using IFEFFIT. *J. Synchrotron. Radiat.* **2005**, *12* (4), 537–541.
(42) Segall, M. D.; Lindan, P. J. D.; Probert, M. J.; Pickard, C. J.; Hasnip, P. J.; Clark, S. J.; Payne, M. C. First-Principles Simulation: Ideas, Illustrations and the CASTEP Code. *J. Phys. Condens. Matter* **2002**, *14* (11), 2717.
(43) Xie, S.; Liu, Z.; Liu, J. Application and Research Status Quo of Material Studio (MS) Software in the Corrosion and Protection. *Comput. Appl. Chem.* **2015**, *2*, 183–187.
(44) Füngerlings, A.; Wohlgemuth, M.; Antipin, D.; Minne, E.van der; Kiens, E. M.; Villalobos, J.; Risch, M.; Gunkel, F.; Pentcheva, R.; Baeumer, C. Crystal-Facet-Dependent Surface Transformation Dictates the Oxygen Evolution Reaction Activity in Lanthanum Nickelate. *Nat. Commun.* **2023**, *14* (1), No. 8284.
(45) Ji, Q.; Bi, L.; Zhang, J.; Cao, H.; Zhao, X. S. The Role of Oxygen Vacancies of ABO_3 Perovskite Oxides in the Oxygen Reduction Reaction. *Energy Environ. Sci.* **2020**, *13* (5), 1408–1428.
(46) Büker, J.; Alkan, B.; Chabbra, S.; Kochetov, N.; Falk, T.; Schnegg, A.; Schulz, C.; Wiggers, H.; Muhler, M.; Peng, B. Liquid-Phase Cyclohexene Oxidation with O2 over Spray-Flame-Synthesized $La_{1-x}Sr_xCoO_3$ Perovskite Nanoparticles. *Chem. Eur. J.* **2021**, *27* (68), 16912–16923.
(47) Bielecki, J.; Svedlindh, P.; Tibebu, D. T.; Cai, S.; Eriksson, S.-G.; Börjesson, L.; Knee, C. S. Structural and Magnetic Properties of Isovalently Substituted Multiferroic $BiFeO_3$: Insights from Raman Spectroscopy. *Phys. Rev. B* **2012**, *86* (18), No. 184422.
(48) Andreasson, J.; Holmlund, J.; Rauer, R.; Käll, M.; Börjesson, L.; Knee, C. S.; Eriksson, A. K.; Eriksson, S.-G.; Rübhausen, M.; Chaudhury, R. P. Electron-Phonon Interactions in Perovskites Containing Fe and Cr Studied by Raman Scattering Using Oxygen-Isotope and Cation Substitution. *Phys. Rev. B* **2008**, *78* (23), 235103.
(49) Sun, S.; Zhang, G.; Yang, Z.; Bai, L.; Li, Y.; Liu, Z.; Xu, J.; Guo, R.; Zhang, Y. Influence of Doped Ions on the Electrochemical Hydrogen Storage Properties of $LaFeO_3$-Based Solid Solutions. *Ceram. Int.* **2024**, *50* (21, Part B), 42176–42187.
(50) Kinetics of Reactions on Surfaces. In *Concepts of Modern Catalysis and Kinetics*; John Wiley & Sons, Ltd , **2003**, pp 267−299.
(51) Davydov, A. A.; Shepotko, M.L.; Budneva, A.A. IR-spectroscopic methods for studying the basic centers of the surface of oxides - analysis of IR-spectra of adsorbed probe-molecule CO_2 as a method for studying basic centers at the surface of oxides. *Kinet. Catal.* **1994**, *35* (2), 272–278.
(52) Busca, G.; Lorenzelli, V. Infrared spectroscopic identification of species arising from reactive adsorption of carbon oxides on metal oxide surfaces. *Mater. Chem.* **1982**, *7*, 89–126(1).
(53) Ramirez, A.; Ticali, P.; Salusso, D.; Cordero-Lanzac, T.; Ould-Chikh, S.; Ahoba-Sam, C.; Bugaev, A. L.; Borfecchia, E.; Morandi, S.; Signorile, M.; Bordiga, S.; Gascon, J.; Olsbye, U. Multifunctional Catalyst Combination for the Direct Conversion of CO_2 to Propane. *JACS Au* **2021**, *1* (10), 1719–1732.
(54) Lavalley, J. C. Infrared Spectrometric Studies of the Surface Basicity of Metal Oxides and Zeolites Using Adsorbed Probe Molecules. *Catal. Today* **1996**, *27*, 377–401.
(55) White, W. B. The Carbonate Minerals. In *The Infrared Spectra of Minerals*; Farmer, V. C., Ed.; Mineralogical Society of Great Britain and Ireland, **1974**, Vol. 4.
(56) Seiferth, O.; Wolter, K.; Dillmann, B.; Klivenyi, G.; Freund, H. J.; Scarano, D.; Zecchina, A. IR Investigations of CO_2 Adsorption on Chromia Surfaces: Cr_2O_3 (0001)/Cr(110) versus Polycrystalline α-Cr_2O_3. *Surf. Sci.* **1999**, *421* (1−2), 176–190.
(57) Schumacher, L.; Weyel, J.; Hess, C. Unraveling the Active Vanadium Sites and Adsorbate Dynamics in VO_x/CeO_2 Oxidation Catalysts Using Transient IR Spectroscopy. *J. Am. Chem. Soc.* **2022**, *144* (32), 14874–14887.
(58) Whitten, A.; Guo, D.; Tezel, E.; Denecke, R.; Nikolla, E.; McEwen, J.-S. Deconvoluting XPS Spectra of La-Containing Perovskites from First-Principles. *JACS Au* **2024**, *4* (8), 3104–3117.
(59) Stoch, J.; Gablankowska-Kukucz, J. The Effect of Carbonate Contaminations on the XPS O 1s Band Structure in Metal Oxides. *Surf. Interface Anal.* **1991**, *17* (3), 165–167.
(60) Stoerzinger, K. A.; Hong, W. T.; Crumlin, E. J.; Bluhm, H.; Biegalski, M. D.; Shao-Horn, Y. Water Reactivity on the $LaCoO_3$ (001) Surface: An Ambient Pressure X-Ray Photoelectron Spectroscopy Study. *J. Phys. Chem. C* **2014**, *118* (34), 19733–19741.
(61) Lukashuk, L.; Yigit, N.; Rameshan, R.; Kolar, E.; Teschner, D.; Hävecker, M.; Knop-Gericke, A.; Schlögl, R.; Föttinger, K.; Rupprechter, G. Operando Insights into CO Oxidation on Cobalt Oxide Catalysts by NAP-XPS, FTIR, and XRD. *ACS Catal.* **2018**, *8* (9), 8630–8641.
(62) Loh, J. Y. Y.; Kherani, N. P. X-Ray Photospectroscopy and Electronic Studies of Reactor Parameters on Photocatalytic Hydrogenation of Carbon Dioxide by Defect-Laden Indium Oxide Hydroxide Nanorods. *Molecules* **2019**, *24* (21), 3818.
(63) Pan, Q.; Peng, J.; Sun, T.; Wang, S.; Wang, S. Insight into the Reaction Route of CO_2 Methanation: Promotion Effect of Medium Basic Sites. *Catal. Commun.* **2014**, *45*, 74–78.
(64) Trost, B. M.; McEachern, E. J. Inorganic Carbonates as Nucleophiles for the Asymmetric Synthesis of Vinylglycidols. *J. Am. Chem. Soc.* **1999**, *121* (37), 8649–8650.
(65) Prakash, G. K. S.; Vaghoo, H.; Panja, C.; Surampudi, V.; Kultyshev, R.; Mathew, T.; Olah, G. A. Effect of Carbonates/Phosphates as Nucleophilic Catalysts in Dimethylformamide for Efficient Cyanosilylation of Aldehydes and Ketones. *Proc. Natl. Acad. Sci. U. S. A.* **2007**, *104* (9), 3026–3030.

https://doi.org/10.1021/acscatal.6c01338
ACS Catal. 2026, 16, 12062−12079

(66) Jia, X.; Zhang, X.; Rui, N.; Hu, X.; Liu, C. Structural Effect of Ni/ZrO_2 Catalyst on CO_2 Methanation with Enhanced Activity. *Appl. Catal., B* **2019**, *244*, 159–169.
(67) Italiano, C.; Llorca, J.; Pino, L.; Ferraro, M.; Antonucci, V.; Vita, A. CO and CO_2 Methanation over Ni Catalysts Supported on CeO_2, Al_2O_3 and Y_2O_3 Oxides. *Appl. Catal., B* **2020**, *264*, No. 118494.
(68) Valange, S.; Beauchaud, A.; Barrault, J.; Gabelica, Z.; Daturi, M.; Can, F. Lanthanum Oxides for the Selective Synthesis of Phytosterol Esters: Correlation between Catalytic and Acid−Base Properties. *J. Catal.* **2007**, *251* (1), 113–122.
(69) Li, X.; Zhao, Z.-J.; Zeng, L.; Zhao, J.; Tian, H.; Chen, S.; Li, K.; Sang, S.; Gong, J. On the Role of Ce in CO_2 Adsorption and Activation over Lanthanum Species. *Chem. Sci.* **2018**, *9* (14), 3426–3437.
(70) Weststrate, C. J.; Sharma, D.; Garcia Rodriguez, D.; Gleeson, M. A.; Fredriksson, H. O. A.; Niemantsverdriet, J. W. Mechanistic Insight into Carbon-Carbon Bond Formation on Cobalt under Simulated Fischer-Tropsch Synthesis Conditions. *Nat. Commun.* **2020**, *11* (1), No. 750.
(71) Cao, J.; Rinaldi, A.; Plodinec, M.; Huang, X.; Willinger, E.; Hammud, A.; Hieke, S.; Beeg, S.; Gregoratti, L.; Colbea, C.; Schlögl, R.; Antonietti, M.; Greiner, M.; Willinger, M. In Situ Observation of Oscillatory Redox Dynamics of Copper. *Nat. Commun.* **2020**, *11* (1), No. 3554.
(72) Biesinger, M. C.; Payne, B. P.; Grosvenor, A. P.; Lau, L. W. M.; Gerson, A. R.; Smart, R. S. t. C. Resolving Surface Chemical States in XPS Analysis of First Row Transition Metals, Oxides and Hydroxides: Cr, Mn, Fe, Co and Ni. *Appl. Surf. Sci.* **2011**, *257*, 2717–2730.
(73) McIntyre, N. S.; Zetaruk, D. G. X-Ray Photoelectron Spectroscopic Studies of Iron Oxides. *Anal. Chem.* **1977**, *49* (11), 1521–1529.
(74) Heijboer, W. M.; Battiston, A. A.; Knop-Gericke, A.; Hävecker, M.; Mayer, R.; Bluhm, H.; Schlögl, R.; Weckhuysen, B. M.; Koningsberger, D. C.; de Groot, F. M. F. In-Situ Soft X-Ray Absorption of Over-Exchanged Fe/ZSM5. *J. Phys. Chem. B* **2003**, *107* (47), 13069–13075.
(75) Szarek, P.; Witkowski, M.; Woźniak, A. P. Unconventional Look at the Diameters of Quantum Systems: Could the Characteristic Atomic Radius Be Interpreted as a Reactivity Measure? *J. Phys. Chem. C* **2019**, *123* (18), 11572–11580.
(76) Ayers, P. W. The Physical Basis of the Hard/Soft Acid/Base Principle. *Faraday Discuss.* **2006**, *135* (0), 161–190.
(77) Atkins, P.; de Paula, J.; Keeler, J. *Atkins' Physical Chemistry*, 12th ed.; Oxford University Press, **2022**.
(78) Vanýsek, P. W.Electrochemical Series. In *Handb. Chem. Phys.*, 93rd ed.; CRC Press, **2012**, pp 5–80.

https://doi.org/10.1021/acscatal.6c01338
ACS Catal. 2026, 16, 12062−12079